International Journal of Coal Geology 191 (2018) 80–94

Contents lists available at ScienceDirect

International Journal of Coal Geology

journal homepage: www.elsevier.com/locate/coal

Raman microspectroscopy, bitumen reflectance and illite crystallinity scale: comparison of different geothermometry methods on fossiliferous Proterozoic sedimentary basins (DR Congo, Mauritania and Australia)

Blaise K. Baludikay[a,*], Camille François[a,*], Marie Catherine Sforna[a], Jérémie Beghin[a], Yohan Cornet[a], Jean-Yves Storme[a], Nathalie Fagel[b], François Fontaine[b], Ralph Littke[c], Daniel Baudet[d], Damien Delvaux[d], Emmanuelle J. Javaux[a]

[a] PPP Lab, GEOLOGY UR & Department, University of Liege, Belgium
[b] AGEs Lab, GEOLOGY UR & Department, University of Liege, Belgium
[c] EMR Group, RWTH Aachen University, Germany
[d] Geodynamics & Mineral Resources Service, Royal Museum for Central Africa, Belgium

ARTICLE INFO

Keywords:
Raman microspectroscopy
Proterozoic organic-walled microfossils
Thermal history
Raman and bitumen reflectances
Illite crystallinity

ABSTRACT

Sedimentary rocks containing microfossils are crucial archives to reconstitute early life evolution on Earth. However, the preservation of microfossils within rocks depends on several physico-chemical factors. Among these factors, the thermal evolution of the host rocks can be decisive. Here, we investigated carbonaceous shale samples containing exquisitely preserved organic-walled microfossils assemblages from three Proterozoic shallow marine sedimentary sequences: the Mbuji-Mayi Supergroup (Democratic Republic of Congo, Congo Basin), the Atar/El Mreïti Group (Mauritania, Taoudeni Basin) and the Kanpa Formation (Australia, Officer Basin). Thermal maturity of these rock samples is evaluated with Raman geothermometry, Raman reflectance, solid bitumen reflectance, illite crystallinity and Thermal Alteration Index. The comparison of results coming from these different techniques validates the use of Raman reflectance on Proterozoic carbonaceous material and especially for poorly-ordered carbonaceous material. We show that extracted kerogen (microfossils and amorphous organic material) is more accurate to estimate the thermal maturity of low-grade temperature Proterozoic sequences than kerogen in thin section. All techniques provide consistent range of temperatures except for Raman geothermometry, giving slightly higher estimates. Raman reflectance appears to be a fast, robust and non-destructive tool to evaluate the thermal maturity of poorly-organized carbonaceous material from Proterozoic rocks.

1. Introduction

Using the microfossil record to reconstruct early life evolution requires the characterization of the physico-chemical conditions of preservation, and the determination of the thermal history of the sedimentary basin in which they were preserved. Initial and post-depositional taphonomic processes during and after fossilization such as burial, biogeochemical degradation, diagenesis, hydrothermal fluid circulation, metamorphism and late contamination may alter or erase the microfossil original properties, challenging the interpretation of the morphology, ultrastructure and geochemistry of the fossil remains, and thus of their biological affinity (Schiffbauer et al., 2012).

In post-Silurian rocks, the thermal maturity of carbonaceous material (CM) and by extension the thermal history of the basins, is usually estimated through the use of the vitrinite reflectance parameter (vR_o%; Littke et al., 2012; Taylor et al., 1998). In pre-Devonian or in marine Paleozoic sedimentary rocks where vitrinite is absent or rare, reflectance data of graptolites (GR_r %), chitinozoans (CR_r %) and scolecodonts (SR_r %) are more often used as a substitute to vitrinite (Bertrand, 1990; Bertrand and Héroux, 1987); However, the application of vitrinite and zooclast (those cited above) reflectance is restricted for Proterozoic sedimentary rocks. This limitation is due to the lack of higher land plants (vitrinite woody precursors) and of these zooclasts among CM encountered in rocks older than the Cambrian (Bertrand and Héroux, 1987; Du et al., 2014; Taylor et al., 1998). As a consequence, solid bitumen reflectance (bR_o%; Albert-Villanueva et al., 2016; Jacob,

* Corresponding authors at: Laboratoire de Paléobiogéologie-Paléobotanique-Paléopalynologie (PPP Lab) Quartier AGORA, Bâtiment B18, Allée du 6 Aout, 14, 4000 Liège (Sart-Tilman), Belgium.
E-mail addresses: bkbaludikay@uliege.be (B.K. Baludikay), francois@uliege.be (C. François).

https://doi.org/10.1016/j.coal.2018.03.007
Received 7 December 2017; Received in revised form 19 March 2018; Accepted 22 March 2018
Available online 27 March 2018

1989; Landis and Castaño, 1995; Riediger, 1993; Schoenherr et al., 2007), the reflectance of non-fluorescent lamalginite (*Ghori in* Stevens and Apak, 1999) as well as the hydrocarbon-based methylphenanthrene index (Radke and Welte, 1983) can be used to estimate an equivalent to vR_0%. Rock-Eval pyrolysis (Espitalié et al., 1977) also allows estimating CM maturity by giving the temperature at which the maximum amount of hydrocarbons is generated from kerogen decomposition (T_{max}). However, Rock-Eval analysis T_{max} depends both on the maturity of a CM and its composition; thus it does not give the maximum temperature reached within a sedimentary basin. Furthermore, it is not useful for rocks which have reached temperatures exceeding 160–200 °C (Peters, 1986; Peters and Cassa, 1994). In fossiliferous rocks, the Thermal Alteration Index (TAI) scale and fluorescence color have been intensively applied (Staplin, 1969). However, the TAI scale is based on palynomorphs wall color that can be affected by the extraction method as well as by the wall thickness, the wall ultrastructure and the wall chemical (Peters and Cassa, 1994; Staplin, 1977). Further details regarding all maturity parameters of CM known in literature as well as different correlations between them have been compiled and discussed in Hartkopf-Fröder et al. (2015). Interested readers could refer to this recent review. In addition to these techniques based on the characterization of CM, the study of the chemical and structural changes in the series smectite/illite-smectite/illite/dioctahedral white mica has been widely used to assess the extent of burial diagenesis and the metamorphic grade of sedimentary successions (Kübler, 1964; Weaver, 1960). Clay minerals are routinely used to determine transition from diagenesis to metamorphism (e.g. Dunoyer de Segonzac, 1969), but the syngenicity of CM preserved in these rocks still need to be evidenced by Raman spectroscopy.

Raman spectroscopy is a fast and non-destructive technique, commonly applied on Precambrian rocks to discriminate CM associated to putative microfossils from void filling, fluid inclusions, migrating CM around minerals, and opaque minerals, but also to determine the thermal maturity of this CM and to evidence its syngenicity (Javaux et al., 2010; Liu et al., 2013; Marshall et al., 2005; Pasteris and Wopenka, 2003). Several geothermometers, from different geological settings of varying thermal and burial histories, based on CM Raman spectral parameters, have been developed to assess peak metamorphic temperatures experienced by host rocks in meteorites or metapelites (Beyssac et al., 2002; Kouketsu et al., 2014; Lahfid et al., 2010; Rahl et al., 2005).

Regional geology and mineral petrology permit to assess qualitatively the degree and type of metamorphism and thermal history of a basin. However, quantitative estimation of thermal maturity of the rocks and CM content is more challenging. Raman geothermometry has never been applied to unambiguous Proterozoic microfossils in order to reconstruct quantitatively the thermal evolution of their host rock, once their syngenicity is evidenced. Raman geothermometry has been calibrated for CM from coal series within metapelites (Beyssac et al., 2003, 2002; Kouketsu et al., 2014; Lahfid et al., 2010) and its use on Proterozoic microfossils need to be validated by independent techniques. Here, after an overlook on several methods, we present the temperature estimates obtained through Raman geothermometry based on spectral parameters (Kouketsu et al., 2014) and on Raman reflectance (Liu et al., 2013) for three Proterozoic sedimentary sequences: the Mbuji-Mayi Supergroup (Congo Basin, Democratic Republic of Congo (DRC)), the Atar/El Mreïti Group (Taoudeni Basin, Mauritania) and the Kanpa Formation (Officer Basin, Australia). We compared measurements obtained on microfossils and amorphous organic matter (AOM), extracted and in situ in thin sections, for these three different sequences. These temperatures were cross-validated with temperature estimates through TAI, solid bitumen reflectance, and 'illite crystallinity Kübler index'.

2. Geological context and samples

2.1. Congo Basin

Localized in Central Africa and covering four countries (Angola, DRC, Central African Republic, and Republic of the Congo), the Congo Basin (Fig. 1a) is an intracratonic basin extending about 1,200,000 km^2. It contains up to 9000 m of sedimentary rocks ranging from late Mesoproterozoic to Neogene and had a complex geological and tectonic evolution (Kadima et al., 2011a, 2011b; Delvaux and Fernandez, 2015). The sedimentary Mbuji-Mayi Supergroup (in the south part of Congo Basin, DRC) was deposited in shallow marine to evaporitic marine and lacustrine environments (Delpomdor et al., 2015). It is considered as equivalent to the basal series of the Congo Basin, buried in the deepest part of the basin and outcropping in the Mbuji-Mayi area due to denudation and rock uplift at the margin of the basin (Delvaux and Fernandez, 2015). This succession is weakly or not at all affected by regional metamorphism (Raucq, 1970) and rests unconformably on the Archean-Paleoproterozoic Congo-Kasai Craton in its southern and western parts, and on the Mesoproterozoic Kibaran Belt in its eastern part (Raucq, 1970). Two distinct lithostratigraphic successions were identified, from the oldest to the youngest: BI Group and BII Group. The BI Group (~500 m thick) is a siliciclastic sequence composed of quartzite, shale, siltstone and some carbonate horizons in its upper part. The BII Group (~1000 m thick) is a carbonate sequence intercalated with thin organic-rich shales and cherts horizons (Delpomdor et al., 2015; Raucq, 1970). Radiometric data constrain the Mbuji-Mayi Supergroup between 1065 and 1030 Ma for the diagenesis of the BI Group to 948 Ma for basaltic lavas which overlie the BII Group, i.e. in the late Mesoproterozoic to early Neoproterozoic (Cahen et al., 1984; François et al., 2017). Several drill cores were performed on the Mbuji-Mayi sedimentary sequence in the 1950's (preserved in the Royal Museum for Central Africa) but only two of them, Kanshi SB13 (425 m-long, Fig. 1a) and Lubi S70 (former Tshinyama S70, 339 m-long, Fig. 1a) cross horizons containing a large diversity of organic-walled microfossils. These drill cores preserve assemblages of organic-walled prokaryotic and eukaryotic microfossils, evidencing the evolution of complex life (early eukaryotes) for the first time in the Meso-Neoproterozoic record of Central Africa (Baludikay et al., 2016). The color of the microfossils and amorphous organic matter in the investigated samples varies from grey brown to dark brown in each sample. We selected one sample per drill core to investigate the thermal maturity of CM. Sample from Kanshi S13B (KN23–123, depth: 123 m) and Lubi S70 (LU18–312, depth: 312 m) drill cores come from the BIIc6 and BIc1 formations, respectively. In sample KN23–123, nine microfossil species and one OAM particle from extracted kerogen were analyzed, as well as two microfossil species and four AOM particles from thin section. In sample LU18–312, two microfossil species and one AOM particle from extracted kerogen were analyzed and in thin section, five microfossil species and one AOM particle (Table 1). The thermal maturity of the Congo Basin is not well-known, especially for the Proterozoic series. Unpublished vitrinite and bitumen reflectance are reported by Lucazeau et al. (2015) for the Mbandaka-1 well in the center of the basin, with a reflectance of 2.56% and modeled temperatures of 160–180° for the deeper part of the well (Neoproterozoic sediments). Vitrinite reflectance have been measured for the Cretaceous – Permian section of the basin (Sachse et al., 2012), with modeled temperatures of 100–120 °C. Recently, Raman microspectroscopy on the asphaltite inclusions within three carbonate samples from upper part of Mbuji-Mayi Supergroup, revealed palaeo-temperatures ranging from 150 to 260 °C (Delpomdor et al., 2018). Thus, the Congo Basin had a long history of sediment accumulation, tectonic inversion, and erosion since the Neoproterozoic (Kadima et al., 2011a; Delvaux and Fernandez, 2015) and is still tectonically active (Delvaux and Barth, 2010), leading to a record of highly disturbed thermal history.

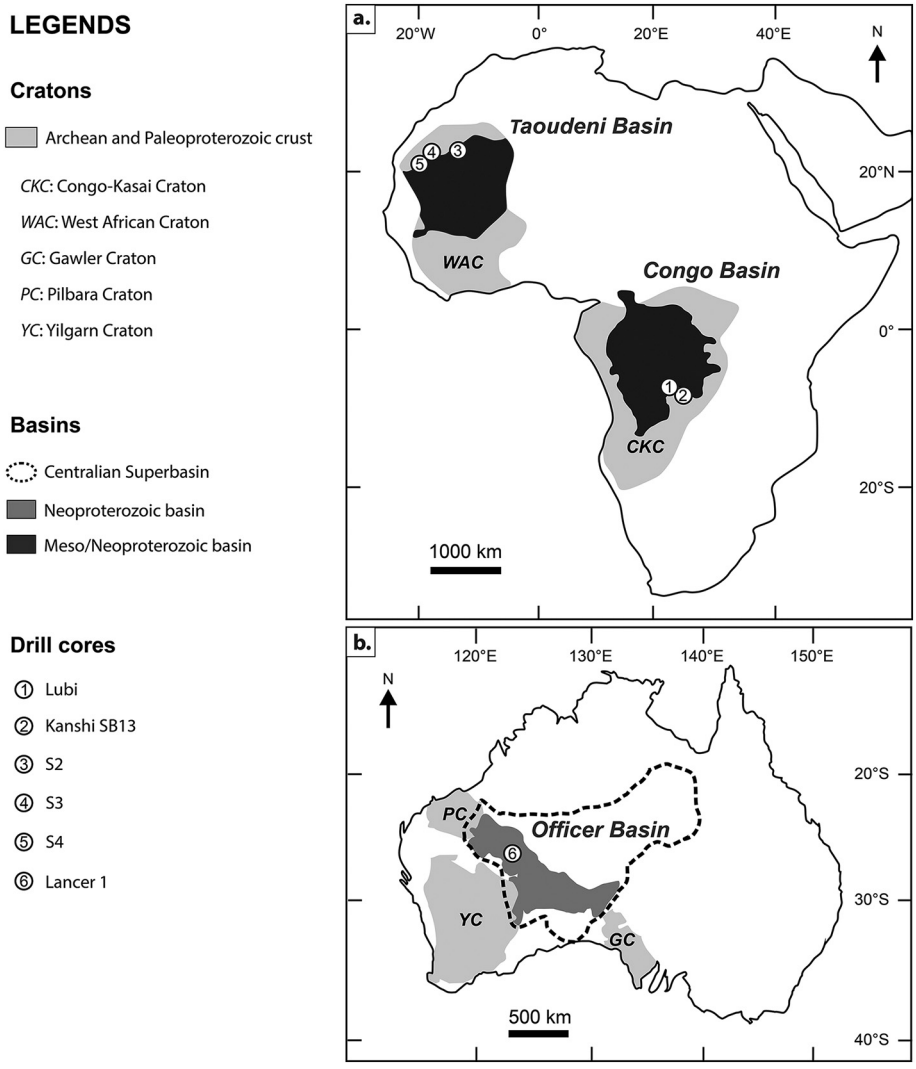

Fig. 1. Simplified geological map of (a) Congo Basin and Taoudeni Basin, and (b) Officer Basin with location of drill cores. Modified after Begg et al. (2009), Camacho et al. (2015) and Kadima et al. (2011a).

2.2. Taoudeni Basin

The Taoudeni Basin (> 1,750,000 km^2; Fig. 1a) is situated in northwestern Africa and extends from Mauritania to northern Mali and western Algeria. This basin is mainly of Proterozoic and Palaeozoic age and contains kilometer-thick (~1500–4000 m) mostly undeformed and unmetamorphosed sedimentary deposits overlying an Archean-Paleoproterozoic basement, the West African Craton (WAC) (Lahondère et al., 2003). The Atar/El Mreïti Group (Mauritania) is a shallow marine deposit of interbedded siliciclastic and carbonate sediments. *Re*—Os geochronology on organic-rich black shales suggests deposition ages of 1107 ± 12 Ma and 1109 ± 22 Ma (Rooney et al., 2010). These ages are supported by the microfossil assemblage composition suggesting a late Mesoproterozoic–early Neoproterozoic age and evidencing the diversification of early eukaryotes in Western Africa (Beghin et al., 2017). Four cores were drilled at the northern margin of the Taoudeni Basin by Total S. A. in 2004 (Rooney et al., 2010). They were named from the East to the West, S1, S2, S3 and S4 (Fig. 1a). S1 was not studied here because it is locally affected by a contact metamorphism resulting from dolerite intrusions. S2 is also not studied, because Raman spectra were unusable due to an intense fluorescence and low signal noise ratio (Fig. A1). A preliminary palynofacies analysis on extracted kerogen from the S2, S3, and S4 cores revealed a wide range of palynomorph colors. In the S2 drill core, the organic matter is translucent light yellow to black opaque via orange and brown in color. This suggests a low maturity of the carbonaceous material. In the S3 and S4 drill cores, organic walls of microfossils and amorphous organic matter are brown and light grey in color, respectively. Rock-Eval analyses on S2 drill core suggest that shales are immature and marginally in the oil-generative window of type II kerogen (Rooney et al., 2010). In contrast, vitrinite equivalent reflectance, vR_oeq % (obtained from bitumen reflectance data, bR_o%) from altered organic-rich shales of the S1 core show a maximum temperature peak of ~288 °C (Rooney et al., 2010). Albert-Villanueva et al. (2016) converted bitumen and pyrobitumen reflectance to vitrinite reflectance equivalent (vR_oeq %) from the R well, which is close to the S4 drill core studied. They obtained vR_oeq % between 0.40 and 1.28% (temperature of 63–87 °C) for bitumen while pyrobitumen gives vR_oeq % range from 1.15 to 3.49% (temperature of 164–312 °C). Martín-Monge et al. (2017) calculated vitrinite reflectance equivalent from the hydrocarbon-based methylphenanthrene index and obtained values between 1.4 and 2% (main gas-generation window) for R1 and R2–R4 wells (corresponding respectively to S3 and S4 drill cores). These authors recognized three episodes of uplift and erosion (Panafrican, Hercynian and Alpine), which created large anticline fault-related structures and subsidence of the Taoudeni Basin. Moreover, ovoid structures related to Mesozoic magmatic intrusions were also recorded. All these events affected the thermal history of the basin. Here, two samples (grey shales) from the S3 and S4 drill cores were selected based

Table 1
Average values of characteristic Raman parameters, Raman reflectance and Raman temperatures. (N) = number acquired spectra; (N′) = number of conserved spectra after initial assessment.

Sample	Location	Geological sequence	Formation	Drill core	Depth (m)	Rock type	Comment	Sample preparation	N	N′	ωD1		ωG		ωG-ωD1	
											Mean	1σ	Mean	1σ	Mean	1σ
KN23-123	Congo Basin	Mbuji-Mayi Supergroup	BIIc6	Kanshi S13B	123	Dark grey shale	AOM	extracted kerogen	10	9	1348.3	2.2	1594.7	2.7	246.4	3.8
							AOM1	Thin section	30	13	1350.9	4.1	1597.5	2.9	246.6	5.6
							AOM2	Thin section	30	17	1348.9	2.7	1596.9	1.7	248.0	2.4
							AOM3	Thin section	30	10	1350.4	2.1	1596.8	2.9	246.4	4.8
							AOM4	Thin section	30	23	1347.4	2.7	1597.4	1.8	250.0	3.2
							Arctacellularia tetragonala	extracted kerogen	12	12	1350.4	1.6	1593.3	2.9	242.9	2.4
							Arctacellularia tetragonala	Thin section	40	22	1351.1	1.9	1598.1	3.2	247.0	3.8
							Leiosphaeridia crassa	extracted kerogen	5	5	1354.4	1.8	1597.0	2.8	242.6	4.0
							Leiosphaeridia crassa1	Thin section	26	13	1350.1	2.7	1599.9	2.5	249.8	3.7
							Leiosphaeridia crassa2	Thin section	31	9	1341.5	1.6	1590.9	1.9	249.4	1.9
							Jacutianema solubila	extracted kerogen	13	13	1351.8	1.4	1595.0	1.8	243.2	1.6
							Leiosphaeridia minutissima	extracted kerogen	14	14	1350.5	0.8	1595.0	2.0	244.5	1.8
							Leiosphaeridia ternata	extracted kerogen	8	6	1343.5	3.0	1589.6	1.8	246.1	3.7
							Polysphaeroides filiformis	extracted kerogen	13	11	1348.7	2.5	1591.5	3.1	242.7	1.9
							Siphonophycus robustum	extracted kerogen	14	12	1349.0	2.7	1594.5	2.4	245.5	2.5
							Spumosina rubiginosa	extracted kerogen	10	9	1346.3	1.5	1589.6	2.0	243.2	2.0
							Synsphaeridium sp.	extracted kerogen	12	12	1348.8	1.4	1589.4	2.4	240.6	1.8
LU18-312	Congo Basin	Mbuji-Mayi Supergroup	BIc1	Lubi	312	Black shale	AOM	extracted kerogen	13	13	1351.0	2.2	1591.5	2.5	240.4	3.1
							AOM	Thin section	10	7	1353.6	1.7	1600.6	1.2	247.0	1.3
							Leiosphaeridia minutissima	extracted kerogen	12	12	1350.4	1.0	1589.9	1.7	239.6	1.7
							Leiosphaeridia minutissima	Thin section	14	8	1351.8	3.3	1597.9	1.7	246.1	3.6
							Leiosphaeridia jacutica	extracted kerogen	11	7	1352.1	2.2	1589.1	2.8	237.0	2.1
							Leiosphaeridia crassa	Thin section	17	14	1351.8	3.4	1597.7	1.4	245.8	3.8
							Leiosphaeridia ternata	Thin section	18	10	1352.2	2.3	1597.5	1.9	245.3	3.5
							Palaeolynbya sp.	Thin section	10	6	1352.3	3.3	1598.0	1.0	245.7	2.7
							Synsphaeridium sp.	Thin section	10	10	1350.3	4.0	1593.3	2.7	243.0	3.8
S3-123	Taoudeni Basin	Supergroup 1 - Hodh	Aguelt el Mabha	S3	123	Grey shale	AOM1	extracted kerogen	35	33	1354.3	2.0	1585.5	1.4	231.2	2.5
							AOM2	extracted kerogen	33	32	1352.8	2.0	1585.0	3.4	232.2	2.9
							Leiosphaeridia crassa1	extracted kerogen	41	36	1352.1	1.6	1584.6	1.6	232.5	2.2
							Leiosphaeridia crassa2	extracted kerogen	15	15	1353.5	2.0	1587.0	1.8	233.5	1.2
							Leiosphaeridia crassa1	Thin section	47	26	1356.9	1.1	1590.4	1.9	233.5	2.3
							Leiosphaeridia crassa2	Thin section	28	27	1355.5	2.7	1592.8	3.3	237.3	4.5
							Synsphaeridium sp.1	extracted kerogen	56	55	1351.2	2.2	1584.3	2.4	233.0	2.0
							Synsphaeridium sp.2	extracted kerogen	9	9	1351.5	2.3	1584.5	1.9	233.1	2.6
							Synsphaeridium sp.1	Thin section	46	18	1356.4	2.5	1591.0	2.5	234.6	3.6
							Synsphaeridium sp.2	Thin section	33	29	1355.9	2.0	1589.6	2.9	233.7	3.5
S4-162	Taoudeni Basin	Supergroup 1 - Hodh	Unit I-3	S4	162	Grey shale	AOM	extracted kerogen	45	41	1346.8	2.3	1591.3	2.5	244.5	2.0
							AOM1	Thin section	27	11	1349.4	1.3	1602.2	1.4	252.8	1.7
							AOM2	Thin section	33	16	1349.6	1.2	1603.3	1.3	253.7	1.5
							AOM3	Thin section	22	14	1349.0	1.8	1601.3	3.6	252.3	5.2
							Leiosphaeridia sp.	extracted kerogen	31	27	1349.2	2.8	1595.9	2.8	246.6	2.8
L1-472	Officer Basin	Supersequence 1	Kanpa	Lancer 1	472	Grey shale	*Cerebrosphaera buickii1*	extracted kerogen	11	11	1355.7	3.3	1580.2	0.7	224.5	3.1
							Cerebrosphaera buickii2	extracted kerogen	12	12	1358.7	1.6	1580.2	0.4	221.5	1.7

(*continued on next page*)

Table 1 (*continued*)

Sample	Location	Geological sequence	Formation	Drill core	Depth (m)	Rock type	Comment	Sample preparation	N	N′	ωD1		ωG		ωG-ωD1	
											Mean	1σ	Mean	1σ	Mean	1σ
L1-680	Officer Basin	Supersequence 1	Kanpa	Lancer 1	680	Grey shale	*Cerebrosphaera buickii1*	extracted kerogen	20	17	1351.7	3.4	1581.3	1.8	229.6	2.7
							Cerebrosphaera buickii2	extracted kerogen	20	19	1349.4	2.0	1581.0	1.5	231.6	2.5
							Cerebrosphaera buickii3	extracted kerogen	20	17	1349.6	3.3	1581.1	1.2	231.5	4.2
							Cerebrosphaera buickii4	extracted kerogen	20	19	1354.5	2.0	1580.4	0.8	225.9	2.4
							Cerebrosphaera buickii1	Thin section	8	7	1359.6	0.8	1589.5	3.3	230.0	3.7
							Cerebrosphaera buickii2	Thin section	20	16	1359.7	0.6	1589.3	3.9	229.6	4.3
							Cerebrosphaera buickii3	Thin section	20	14	1359.4	1.2	1589.0	3.5	229.6	3.3
L1-955	Officer Basin	Supersequence 1	Kanpa	Lancer 1	955	Grey shale	*Cerebrosphaera buickii1*	extracted kerogen	20	17	1354.4	3.2	1582.1	2.4	227.7	3.4
							Cerebrosphaera buickii2	extracted kerogen	20	17	1355.9	3.7	1583.5	4.2	227.6	3.1
							Cerebrosphaera buickii1	Thin section	20	20	1355.1	3.7	1593.0	3.0	237.9	5.1
							Cerebrosphaera buickii2	Thin section	20	20	1354.2	3.9	1587.6	2.9	233.4	6.1

Sample	FWHM-D1		FWHM-G		FWHM-D1/FWHM-G		ID1		IG		ID1/IG		R_mcR_0 %		T (FWHM-D1) (°C)		T (R_mcR_0%) (°C)	
	Mean	1σ	Mean	1σ	Mean	1σ	Mean	1σ	Mean	1σ	Mean	1σ	Mean	1σ	Mean	1σ	Mean	1σ
KN23-123	108.0	5.8	53.1	3.7	2.04	0.11	171.4	24.9	321.4	48.1	0.53	0.04	2.02	0.21	246	12	192	8
	107.8	3.7	51.3	3.8	2.11	0.13	3442.7	4353.7	6634.2	8948.2	0.58	0.13	2.03	0.30	246	8	192	11
	110.2	4.7	53.1	1.8	2.07	0.07	11164.4	2403.8	21002.4	4545.6	0.53	0.04	2.11	0.13	241	10	195	5
	101.3	5.6	48.0	3.5	2.13	0.24	1086.0	1230.0	1829.9	2141.1	0.61	0.07	2.02	0.26	260	12	192	10
	107.9	4.9	50.8	3.6	2.13	0.17	4170.7	3862.1	6732.6	6431.2	0.62	0.06	2.22	0.17	246	10	199	6
	109.2	3.4	55.0	3.9	1.99	0.13	821.7	500.4	1613.9	981.9	0.51	0.02	1.83	0.13	243	7	184	6
	113.0	4.9	54.4	4.3	2.09	0.14	8406.7	2796.5	14837.7	5929.7	0.58	0.07	2.06	0.20	235	10	193	8
	107.4	4.8	52.6	3.2	2.05	0.07	146.1	20.1	270.4	52.5	0.55	0.06	1.82	0.21	247	10	183	10
	112.3	5.4	54.4	4.9	2.08	0.20	7941.0	1929.2	13854.5	3732.3	0.58	0.04	2.20	0.20	236	12	199	7
	112.7	7.9	57.4	3.3	1.96	0.11	4398.2	1041.3	7283.3	2319.1	0.62	0.07	2.18	0.10	236	17	198	4
	109.6	3.1	54.8	1.9	2.00	0.06	1101.8	202.4	2058.1	400.4	0.54	0.03	1.85	0.09	242	7	185	4
	107.2	2.9	54.0	2.4	1.99	0.10	1000.0	212.7	1930.1	447.2	0.52	0.03	1.92	0.09	247	6	188	4
	110.1	6.8	56.8	1.9	1.94	0.16	145.3	81.1	256.7	136.2	0.55	0.04	2.01	0.20	241	15	191	8
	107.2	3.9	53.5	4.2	2.01	0.11	229.6	35.1	437.7	77.1	0.53	0.02	1.82	0.10	248	8	184	5
	105.4	4.9	50.9	2.8	2.08	0.16	523.4	175.1	979.9	317.4	0.53	0.02	1.97	0.14	251	11	190	5
	110.4	4.1	58.1	3.6	1.90	0.08	272.6	65.8	488.4	122.5	0.56	0.03	1.85	0.11	241	9	185	5
	112.0	3.1	60.0	4.1	1.87	0.09	523.4	175.1	979.9	317.4	0.53	0.03	1.71	0.10	237	7	179	5
LU18-312	113.5	3.1	58.6	2.6	1.94	0.09	929.9	306.9	1484.7	509.6	0.63	0.03	1.70	0.17	234	7	178	8
	117.2	6.9	57.0	5.4	2.08	0.29	5882.4	954.1	8708.3	1371.7	0.68	0.09	2.05	0.07	226	15	193	3
	112.6	3.0	59.4	2.1	1.90	0.06	642.9	191.7	1111.6	341.0	0.58	0.03	1.66	0.09	236	6	176	4
	120.1	3.4	60.5	2.3	1.99	0.11	7078.3	1743.6	11139.0	3052.8	0.64	0.06	2.01	0.19	220	7	191	8
	111.4	4.1	58.0	2.0	1.92	0.08	209.4	70.6	394.8	135.4	0.53	0.04	1.52	0.11	239	9	169	6
	119.4	6.0	58.6	3.1	2.04	0.14	8700.4	1234.8	12888.4	1841.2	0.68	0.06	1.99	0.20	221	13	191	8
	119.8	4.1	60.5	3.3	1.98	0.09	7678.7	1525.2	11434.5	2580.8	0.68	0.06	1.96	0.19	220	9	190	7
	120.6	2.5	56.9	1.3	2.12	0.06	10277.1	1465.9	16121.1	2138.4	0.64	0.03	1.98	0.14	219	5	191	6
	123.2	10.7	58.0	2.4	2.12	0.14	12010.2	2089.7	19666.3	4347.7	0.62	0.04	1.84	0.20	213	23	184	9
S3-123	123.2	5.3	70.2	3.1	1.76	0.08	421.9	115.2	596.5	151.6	0.71	0.03	1.20	0.13	213	11	150	8
	120.2	5.2	66.6	4.0	1.81	0.16	1390.0	811.7	1784.0	898.4	0.76	0.08	1.26	0.16	220	11	153	10
	121.7	3.7	69.5	2.7	1.75	0.07	547.4	143.2	835.1	215.4	0.66	0.03	1.27	0.12	216	8	155	7
	118.0	2.1	64.8	2.9	1.82	0.06	727.5	176.7	1113.5	273.3	0.66	0.05	1.33	0.07	224	5	158	4
	124.9	3.7	63.5	1.7	1.97	0.08	1920.8	659.3	2962.3	845.6	0.64	0.07	1.33	0.12	210	8	158	8
	127.3	4.9	69.3	3.8	1.84	0.12	2301.8	589.2	3064.4	777.5	0.75	0.06	1.53	0.24	204	10	169	13
	122.3	4.2	69.6	3.6	1.76	0.07	407.2	99.7	643.5	159.1	0.63	0.03	1.30	0.11	215	9	157	7
	121.6	3.8	71.1	3.5	1.71	0.06	314.6	79.1	501.9	117.8	0.62	0.03	1.31	0.14	217	8	157	8
	120.5	6.6	65.5	3.6	1.85	0.15	1032.4	615.5	1347.3	811.7	0.77	0.06	1.39	0.19	219	14	161	11
	126.1	4.4	64.9	4.8	1.96	0.19	2629.4	712.8	3356.4	886.2	0.78	0.07	1.34	0.19	207	10	158	12

(*continued on next page*)

Table 1 (*continued*)

Sample	FWHM-D1		FWHM-G		FWHM-D1/FWHM-G		ID1		IG		ID1/IG		R_mcR_0 %		T (FWHM-D1) (°C)		T (R_mcR_0%) (°C)	
	Mean	1σ	Mean	1σ	Mean	1σ	Mean	1σ	Mean	1σ	Mean	1σ	Mean	1σ	Mean	1σ	Mean	1σ
S4-162	113.1	4.7	53.8	3.4	2.11	0.13	745.8	301.9	1312.7	576.5	0.58	0.06	1.92	0.11	235	10	188	5
	104.3	2.2	40.1	2.2	2.61	0.19	5035.1	1231.2	9290.6	2254.8	0.54	0.05	2.37	0.09	254	5	205	3
	106.3	3.8	45.4	1.9	2.34	0.08	2090.2	1103.7	3970.2	1817.6	0.52	0.04	2.41	0.08	250	8	207	3
	105.3	5.5	45.2	7.1	2.36	0.24	2232.5	1816.7	4265.3	3603.3	0.53	0.04	2.34	0.28	252	12	203	12
	112.2	8.1	49.6	6.2	2.28	0.21	2020.6	909.1	3741.5	1844.5	0.56	0.07	2.03	0.15	237	17	193	6
L1-472	135.5	4.6	84.3	2.3	1.61	0.07	1181.6	118.9	1526.0	144.2	0.78	0.06	0.85	0.17	187	10	121	15
	144.2	3.7	87.6	1.9	1.65	0.02	1387.0	102.8	1822.1	154.6	0.76	0.03	0.68	0.09	168	8	104	10
L1-680	137.3	9.1	79.6	3.4	1.73	0.15	727.7	161.7	1022.9	210.8	0.71	0.07	1.12	0.15	183	20	144	10
	141.2	11.4	77.9	1.9	1.81	0.13	1265.8	231.1	1631.7	272.0	0.78	0.07	1.23	0.14	174	24	151	9
	147.2	10.8	77.6	2.2	1.90	0.12	1244.2	177.2	1610.3	203.2	0.77	0.06	1.22	0.23	161	23	150	16
	129.2	3.2	78.1	2.6	1.66	0.05	870.6	430.4	1194.3	538.6	0.72	0.03	0.92	0.13	200	7	128	10
	133.3	6.6	80.7	3.0	1.65	0.03	4473.5	1125.3	6096.6	1857.7	0.75	0.07	1.14	0.20	191	14	145	14
	136.5	11.2	81.6	4.8	1.67	0.06	4170.4	1650.6	5831.3	2627.7	0.73	0.06	1.12	0.23	184	24	143	16
	135.5	6.5	80.0	3.9	1.70	0.08	5520.4	1577.3	6962.8	2621.7	0.82	0.09	1.12	0.18	187	14	144	12
L1-955	133.6	6.3	78.5	4.0	1.70	0.11	1073.5	315.5	1273.4	339.2	0.84	0.08	1.02	0.18	191	13	136	14
	138.1	7.3	89.0	6.0	1.55	0.09	574.2	122.6	756.0	155.6	0.76	0.09	1.01	0.17	181	16	135	14
	139.4	5.4	86.1	3.7	1.62	0.08	24621.5	3363.3	34098.1	4483.3	0.72	0.07	1.57	0.27	178	12	170	15
	142.6	10.3	81.2	3.9	1.76	0.07	23307.1	3731.2	24592.7	5970.0	0.96	0.09	1.32	0.33	172	22	156	20

on an assemblage including fossil eukaryotes (Beghin et al., 2017). Sample from the S3 drill core comes from the Aguelt el Mabha Formation (S3–123, depth: 123 m) and sample from the S4 core comes from the Unit I-3 (S4–162, depth: 162 m). In sample S3–123, two microfossil species both from extracted kerogen and from thin section were analyzed, in addition to two AOM particles from extracted kerogen. In sample S4–162, one microfossil species and one AOM particle from extracted kerogen; and three AOM particles from thin section were analyzed (Table 1). Although Raman spectra from S2 drill core were unusable as mentioned above, one sample (green grey shale) from the Khatt Formation (S2–216, depth: 216 m) was characterized by XRD analyses and Thermal Alteration index (Table 2).

2.3. Officer Basin

The Officer Basin (Fig. 1b) is a part of the Centralian Superbasin, located in Western and Central Australia, an intracratonic basin of ~2,000,000 km^2 formed during the breaking-up of the Supercontinent Rodinia (Walter et al., 1995). The Centralian Superbasin is divided into 7 sub-basins, one of which is the Officer Basin. It is situated between the Yilgarn and Pilbara Craton in the West, the Gawler Craton in the Southeast and the Musgrave Orogenic Block in the North (Stevens and Apak, 1999) and recorded a quite long geological period with 1500 to 4000 m of sedimentary deposits. Ages range from the Tonian (1000–720 Ma) to the mid-Carboniferous (deduced from the palynological content) in most part of the basin (Grey et al., 2011). In addition, some areas also contain Cretaceous deposits (Mory and Haines, 2005; Stevens and Apak, 1999). The Centralian Superbasin is divided into four successive Supersequences (1 to 4). The Supersequence 2 is not recorded in the Officer Basin. The Supersequence 1 is principally composed of sandstone, dark mudstone and dolomite with small patches of siltstone and evaporites. It records shallow marine up to coastal and sabkha conditions and is composed, from bottom to top, of the Lefroy, Browne, Hussar and Kanpa formations. The basement of Centralian Superbasin, as the whole basin, is poorly dated with a K−Ar age of 1058 ± 13 Ma (Mory and Haines, 2005). We focused on the Lancer 1 drill core in the west (Fig. 1b), which intercepts the whole Supersequence 1 and shows a wide microfossil diversity in the shaly horizons of the Hussar (494.1 m-thick) and Kanpa (241 m-thick) formations (Mory and Haines, 2005*)*. Both contain the acritarch *Cerebrosphaera* (Cotter, 1997), an index microfossil of the Tonian period (Grey et al., 2011; Mory and Haines, 2005). Within the three rock samples of the Kanpa Formation that were investigated, we analyzed two specimen of *Cerebrosphaera* from extracted kerogen of sample L1–472 (depth: 472 m); four specimen from extracted kerogen and three specimen in thin section from sample L1–680 (depth: 680 m) as well as two specimen from extracted kerogen and two specimen in thin section from sample L1–955 (depth: 955 m). Interestingly, all studied *Cerebrosphaera* specimens show a variety of organic wall color ranging from a very light-brown to a mid-brown up to a dark brown color. A variable opacity can also be observed on the specimen, with some specimens showing a high transparency while others are entirely opaque. No temperature estimate has been attempted for the Lancer 1 in previous studies. However, analyses have been carried out for Empress 1A, a drill core situated 200 km north-west of the Lancer 1 drill core and crossing the Supersequence 1 and especially the Kanpa Formation. Temperatures comprised between ~120 °C and ~140 °C at minimum were obtained through the reflectance of non-fluorescent lamalginite converted to vitrinite equivalent reflectance (0.52 and 1%; *Ghori in*Stevens and Apak, 1999). The Keene basalt intrusion inside the Kanpa Formation, in the Lancer 1 drill core at a depth of 527.3 to 576.2 m (*Pirajno in*Mory and Haines, 2005), most probably influenced the temperature recorded into the sediments.

Table 2
Compilation of mean temperatures calculated from Raman spectral parameters, solid bitumen reflectance together with TAI scale and KI for all samples (extracted kerogen and thin section).

		Data from Raman parameters						Data from solid bitumen				Calculated temperatures						Data from XRD		
Sample	Sample preparation	FWHM-D1		ωG-ωD1		$RmcR_0$ %		bR_0 %		vR_0 eq %		Tpeak from vR_0 eq (°C)		Tpeak from $RmcR_0$ %		T° from FWHMD1 (°C)		TOC (wt %)	TAI scale	Kübler index (Δ°2θ)	KI domain
		Mean	1σ	Mean	1σ	Mean	1σ	Mean	1σ	Mean	1σ	Mean	1σ	Mean	1σ	Mean	1σ				
KN23-123	Extracted kerogen	108.6	4.4	243.7	2.9	1.87	0.15	2.28	0.16	2.46	0.15	208	5	186	7	244	9	0.4	3/3+	0.82	Diagenesis
	Thin section	109.3	6.1	248.4	3.9	2.13	0.21							196	8	243	13				
LU18-312	Extracted kerogen	112.7	3.3	239.4	2.7	1.64	0.15	2.22	0.15	2.41	0.14	206	5	175	7	236	7	0.5	3+/4-	0.57	Diagenesis
	Thin section	120.1	6.4	245.4	3.4	1.97	0.18							190	8	220	14				
S2-216	–	–	–	–	–	–	–	–	–	–	–	–	–	–	–	–	–	–	2+/2	1.48	Diagenesis
	–	–	–	–	–	–	–							–	–	–	–				
S3-123	Extracted kerogen	121.6	4.6	232.5	2.4	1.27	0.13	–	–	–	–	–	–	155	8	217	10	–	3	0.98	Diagenesis
	Thin section	125.1	5.3	234.8	3.8	1.40	0.21							162	12	209	11				
S4-162	Extracted kerogen	112.7	6.2	245.4	2.6	1.97	0.14	–	–	–	–	–	–	190	6	236	13	–	3	0.48	Diagenesis
	Thin section	105.4	4.1	253.0	3.3	2.38	0.18							205	7	251	9				
L1-472	Extracted kerogen	140.1	6.1	222.9	2.9	0.76	0.15	–	–	–	–	–	–	112	15	177	13	–	3-/3	1.23	Diagenesis
L1-680	Extracted kerogen	138.5	11.1	229.6	3.8	1.12	0.20	–	–	–	–	–	–	143	15	180	24	–	3	0.87	Diagenesis
	Thin section	135.5	8.7	229.7	3.8	1.12	0.20							144	14	187	19				
L1-955	Extracted kerogen	135.6	7.1	227.7	3.2	1.01	3.25	–	–	–	–	–	–	136	14	186	15	–	3-/3	–	–
	Thin section	141.0	8.3	235.7	6.01	1.44	0.32							163	19	175	18				

3. Proxies for temperature and maturity of CM estimates

Note that the use of the term “maturity” differs from one proxy to another. In Raman spectroscopy, the increase of CM maturity corresponds to the increase of crystallinity, i.e. the aromatization of CM and the decrease of defects. In the petroleum domain (where TAI scale, vitrinite and solid bitumen reflectance are used), the term maturity refers not only to chemical and physical properties of CM but also to petroleum potential of CM (or organic matter), i.e. its capacity to generate hydrocarbons (oil and gas).

3.1. TAI scale

TAI scale has been traditionally used by palynologists in the petroleum industry to quickly assess the maturity of CM and the temperature that affected CM based on the comparison of palynomorphs present in the samples to a standard color scale, (Fig. A2). Its application can nonetheless be limited as color estimation can be subjective. Moreover, the published scale (Staplin, 1977) was established with laboratory experiments on one or a few types of palynomorphs (mostly spores) and thus is restricted to a certain number of palynomorph types, which are not always present in the investigated sample (Szczepanik, 1997) nor relevant for the Precambrian. Moreover, organic-walled microfossil assemblages commonly include taxa displaying different wall color. Despite their similar taphonomic history, co-occurring taxa may differ in color due to several factors such as the wall thickness, the wall ultrastructure, the wall chemical composition, the wall ornamentation, the intensity of the microscope light, and the overlapping of folds in the specimens darkening the transmitted light. The very simple approach of the TAI permits a practical and quick first assessment of thermal maturity but has strong limitations and does not take into account these effects. To illustrate this idea, a filter with a transparency of 50% applied on the value 2- in the TAI scale correspond to the color of the value 1 (Fig. A2). To use the TAI scale in a more objective way (as much as possible with human eyes), we propose a new pattern of the TAI scale (color codes in Munsell color and RGB systems Fig. A2) showing the different percent of transparency for a same value in the traditional TAI scale (Fig. A2). To use this scale, the observer must determine the value of the TAI scale in an area not displaying folds or inclusions and has to work on a large variety of specimens to obtain a clear overview of the color range of the specimen.

3.2. CM Raman spectrum and Raman geothermometry

In an ideal graphite crystal, only one band is Raman active at 1580 cm^{-1}. This band, called G-band, corresponds to in-plane stretching vibration of the aromatic carbon (E_{2g} vibration, e.g. Nemanich and Solin, 1979). In natural CM two additional bands arise. One is centred at 1350 cm^{-1} and another forms a shoulder on the G-band at ca. 1620 cm^{-1}, called D1- and D2-band respectively (Fig. A3, Wopenka and Pasteris, 1993). These two bands correspond to in-plane breathing vibration made possible by the defect in the ideal graphitic structure. Supplementary bands can form shoulders on the D1-band at 1500 cm^{-1} and 1190–1250 cm^{-1}, called D3- and D4-band, respectively, when the crystallinity of the CM is low (Lahfid et al., 2010). The D3-band results from out-of-plane vibration of tetrahedrally coordinated carbons, dangling bonds and heteroatoms (Beyssac et al., 2002; Wopenka and Pasteris, 1993). The D4-band that occurs only in CM with a very low crystallinity has a more discussed origin but could result from the vibration of C—C in polyene structure (Dippel et al., 1999).

CM Raman spectra have been used as proxies to estimate peak metamorphism temperature. The thermal alteration of CM is non-reversible and the evolution of the spectral parameters (Fig. A3) such as peak intensity (I_{D1}, I_{D2}, I_{D3}, I_{D4} and I_G), peak area (A_{D1}, A_{D2}, A_{D3}, A_{D4} and A_G) and peak full width at half maximum (FWHM-D1, FWHM-D2,

FWHM-D3, FWHM-D4, and FWHM-G), as well as the evolution of their ratio, are strongly linked to the crystallinity of the CM (Ferrari and Robertson, 2000; Kouketsu et al., 2014; Wopenka and Pasteris, 1993). Empiric geothermometers, based on the different spectral parameters, have been proposed to estimate peak temperature underwent by CM within metapelites for precise temperature ranges (Beyssac et al., 2002; Rahl et al. (2005); Lahfid et al., 2010; Kouketsu et al., 2014). With the exception of Kouketsu et al. (2014) thermometers, all of the other thermometers have been calibrated for temperature above 200 °C. However, the fitting protocol and the subtraction of baseline due to the background fluorescence are critical parameters for a coherent estimation of the temperature (Lünsdorf et al., 2014). Based on the known geological context of our study sites, we thus decided to apply only the more relevant thermometers established by Kouketsu et al. (2014) based on width of D1-band (FWHM-D1, Eq. 1) or the width of D2-band (FWHM-D2, Eq. 2). Due to the difficulty to identify correctly the D2-band, we estimated temperature only with the thermometer based on FWHM-D1 (Eq. 1).

$$T\,(^{\circ}C) = -2.15^{*}FWHM - D1 + 478 \quad (1)$$

$$T\,(^{\circ}C) = -6.78^{*}FWHM - D2 + 535 \quad (2)$$

3.3. Estimates of temperature from reflectance

Vitrinite is a maceral group derived from terrigenous (woody) CM occurring in post-Silurian sedimentary rocks. Its reflectance, *vRo %*, (*or VR*; Taylor et al., 1998) can be used as indicator of the thermal maturity as it increases with temperature (Barker and Pawlewicz, 1994; Jasper et al., 2009; Zieger et al., 2018). It has been widely used to study the thermal evolution of sedimentary basins and for oil and gas exploration (Barker and Pawlewicz, 1994). Barker and Pawlewicz (1994) proposed a calibrated geothermometer, Vitrinite Reflectance Geothermometer (VRG), allowing the estimate of the peak temperature underwent within sedimentary basins in both burial ($T_{peak\ burial}$, Eq. 3) and hydrothermal ($T_{peak\ hydrothermal}$, Eq. 4) settings.

$$T_{peak\ burial}\,(^{\circ}C) = (\ln(vR_0\%) + 1.68)/0.0124 \quad (3)$$

$$T_{peak\ hydrothermal}\,(^{\circ}C) = (\ln(vR_0\%) + 1.19)/0.00782 \quad (4)$$

For rocks devoid of vitrinite, the use of solid bitumen reflectance have been proposed (bR_0%; Jacob, 1989; Landis and Castaño, 1995; Riediger, 1993) or Raman reflectance ($RmcR_0$%; Liu et al., 2013; Sauerer et al., 2017), which can be successively used in the VRG equations (Liu et al., 2013).

Solid bitumen is a residual product of thermal conversion of kerogen in organic-rich mature and post-mature rocks (Landis and Castaño, 1995). Bitumen is part of CM partly migrating in rocks and forming oil, thus it is often not syngenetic to the hosting rock. However, when solidified (sometimes called “pyrobitumen”), it is not mobile anymore and its maturity should reflect the temperature undergone by the hosting rock and co-occurring syngenetic CM such as primary macerals or organic microfossils. Solid bitumen occurs in three optical forms, (1) “anisotropic coked” exhibiting a bright reflective appearance with a strong anisotropy, (2) “granular”, and (3) “homogeneous”. Only the homogeneous variety is recommended for thermal history studies due to its weak anisotropy and its wider distribution (Landis and Castaño, 1995). In addition, it is extremely difficult to confound this type of solid bitumen with other organic constituents. Different equations have been proposed to obtain an equivalent to vitrinite reflectance (vR_0eq %) from solid bitumen reflectance for different lithologies (Jacob, 1989; Landis and Castaño, 1995; Riediger, 1993; Schoenherr et al., 2007). We used here the equation that has been determined from rocks with a low permeability such as shales and siltstones (Landis and Castaño, 1995, Eq. 5).

$$vR_0\ eq\% = (bR_0\% + 0.41)/1.09, \quad (5)$$

Raman reflectance ($RmcR_0$%) has been defined as an equivalent of vitrinite reflectance based on the linear correlation of vR_0% with the distance between the D1- and G- band positions (ωG–ωD1, Eq. 6, Liu et al., 2013) for mature to highly mature samples and with or the intensity ratio of G and D1-bands (I_{D1}/I_G) for post-mature samples (Eq. 7, Liu et al., 2013). We introduced the different vR_0eq % values in the VRG equation defined for burial settings as no evidence for hydrothermalism was observed in our samples.

$$RmcR_0\% \equiv vR_0\ eq\% = 0.0537^{*}(\omega G - \omega D1) - 11.21 \text{ for mature to highly mature samples} \quad (6)$$

$$RmcR_0\% \equiv vR_0\ eq\% = 1.1659^{*}(I_{D1}/I_G) + 2.7588 \text{ for post - mature samples} \quad (7)$$

3.4. Illite crystallinity (IC)

Diagenetic clay minerals usually occur as heterogeneous assemblages of submicroscopic layers of different structure types such as illite, smectite, vermiculite and chlorite. The nature of the assemblage and the crystallinity of illite vary as a function of the temperature. Illite crystallinity (IC) has been applied mainly to detect the transition zone between diagenesis and very low-grade metamorphism (Kübler, 1967). The IC currently named Kübler-Index (KI; Guggenheim et al., 2002) corresponds to an indirect measurement of the mean consecutive illite layers contained in coherent scattering domains of mixed-layer illite-smectite (Kübler and Jaboyedoff, 2000). It is obtained by measuring the full width at half maximum height (FWHM) of the 10 Å-illite X-ray peak in the air dried preparation, when for conceptual reasons it is admitted that expandable mixed-layers contain only illite s.s. or that expandable mixed-layers were removed by treatment (Ferreiro Mählmann et al., 2012; Ferreiro Mählmann and Frey, 2012; Kübler and Jaboyedoff, 2000; Warr and Rice, 1994). However, in nature, this representative trend in smectite-free sample is not very frequent (Ferreiro Mählmann et al., 2012). Hence, for samples with discrete smectite content, KI corresponds in fact to FWHM of the 10 Å X-ray diffraction peak of illite/smectite mixed-layer (I/S) in the ethylene-glycol treated preparation (Jaboyedoff et al., 2000; Jaboyedoff et al., 2001; Kübler and Jaboyedoff, 2000). KI is typically reported in units of Δ°2θ Cu Kα. Its value decreases with rising metamorphic conditions. Several KI values were proposed in the past but, two KI calibrations are recommended (Warr and Ferreiro Mählmann, 2015): (i) from Kübler's original standards (Kübler, 1967) and (ii) from Crystallinity Index Standards (CIS, Warr and Rice, 1994). A correlation was established between these two KI calibrations, for a better compatibility of published data from different laboratories. According to Kübler's original calibration, the diagenesis zone is characterized by KI up to 0.42 Δ°2θ, the anchizone by value between 0.42 and 0.25 Δ°2θ and the epizone by KI lower than 0.25 Δ°2θ. While, for KI values determined using the CIS calibration, the equivalent limits of the anchizone are 0.32 and 0.52°2θ (Warr and Ferreiro Mählmann, 2015). These three metamorphic zones roughly correspond to temperatures lower than 200 °C, 200 to 300 °C, and above 300 °C, respectively. Here we use the Kübler's original scale (also called KF scale, Warr and Ferreiro Mählmann, 2015) to define temperatures ranges undergone by the samples.

4. Methods

4.1. Raman spectroscopy

Samples were prepared at the University of Liège (PPP Laboratory, UR GEOLOGY, Belgium) through two preparation methods prior to Raman measurements: acid maceration (isolated kerogen) and thin section (Fig. 2 and Table 1). Both methods were performed on all samples from Congo (two samples: KN23–123and LU18–312), Taoudeni (two samples: S3–123 and S4–162) and Officer (three samples:

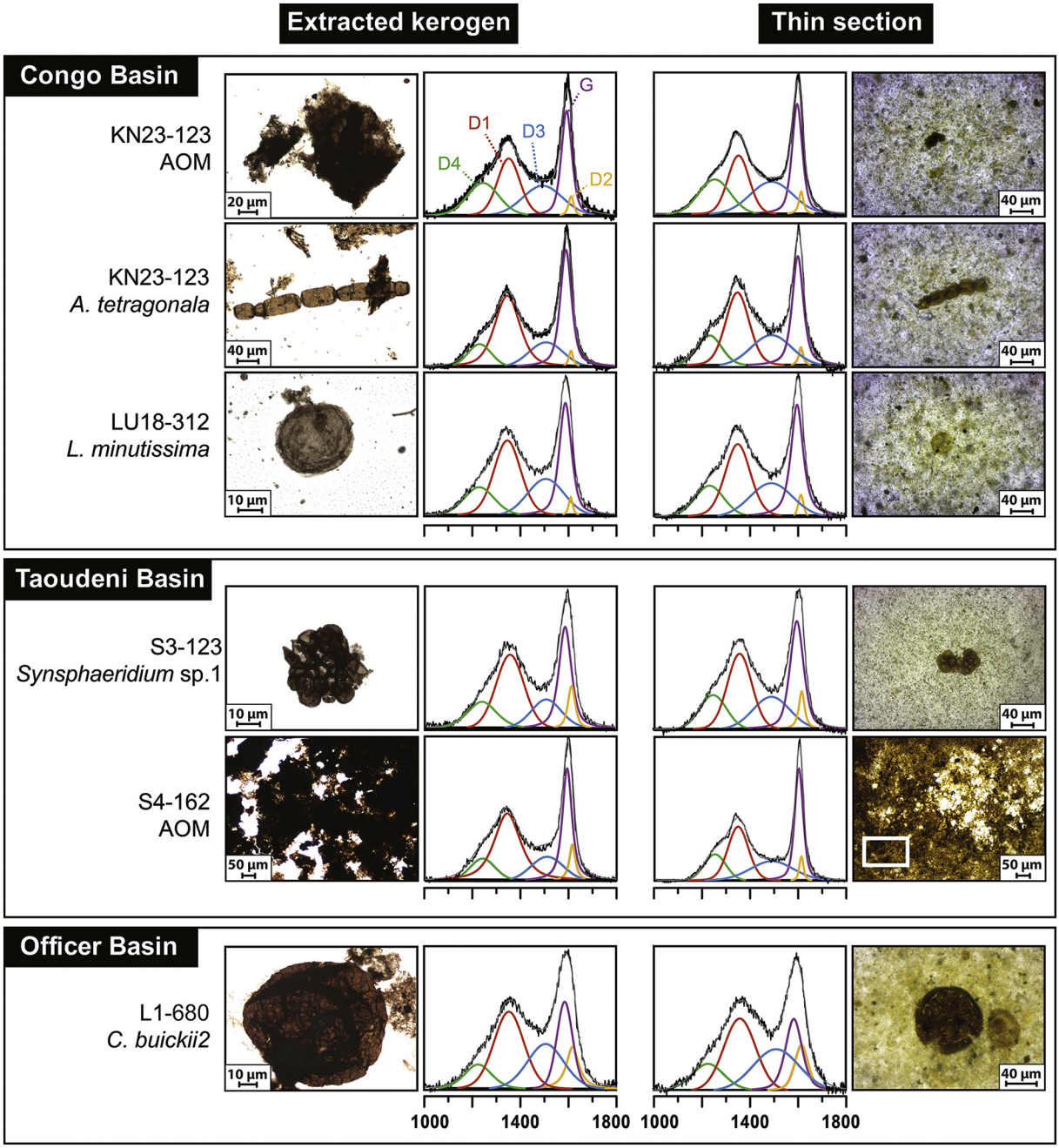

Fig. 2. Photomicrographs of some AOM and microfossils in extracted kerogen (left) and in thin section (right) in studied drill cores from the three basins and corresponding representative Raman deconvoluted spectra.

L1–472, L1–680, L1–955) basins.

The kerogen (microfossils and AOM) was extracted following a modified preparation procedure described by Grey (1999). After cleaning, samples were crushed in a mortar. Carbonates were removed by hydrochloric acid (HCl, 35%) and silicates by hydrofluoric acid (HF, 60%). Neo-formed fluorides were removed by hot HCl. The organic fraction was filtered by hand. Centrifugation that could damage fragile fossilized forms and oxidation that can alter kerogenous wall chemistry and color were avoided. Extracted kerogen was stored in millipore water. For Raman preparation, extracted kerogen was pipetted under an inverted microscope and dropped on standard microscope slides for at least one week drying before Raman analysis.

For preparing the thin sections, a thin sliver parallel to the stratification plane was cut with a diamond saw, allowing the observation of microfossils. This thin sliver was put in an oven at 60 °C for 1 day. After drying, it was mounted on a glass slide by cold bonding with epoxy resin (< 60 °C to not affect the carbonaceous material). The thickness of the sample was reduced to 30 µm with progressively finer abrasive grit (9, 6, 1, ¼ µm) to obtain a mirror polishing.

Raman analyses were performed on a Renishaw Invia Raman microspectrometer at the University of Liège (PPP Laboratory, UR GEOLOGY, Belgium) with an Ar-ion-40 mW monochromatic 514 nm laser source. Laser excitation was focused through a 50× objective to obtain a 1–2 µm spot size and laser power at the sample surface was set at around 2 mW. Acquisitions were made in "Mapping point"-mode, with a 1800 l/mm grating, a 100 cm^{-1} cut-off edge filter and a 1040 × 256 pixel CCD array detector. This allowed the acquisition of Raman spectra with a 2000 cm^{-1} detection range and a 4 cm^{-1} spectral resolution. Beam centering and Raman spectra calibration was performed on a Si glass with a characteristic Si-band at 520.4 cm^{-1}. In

"Mapping-point" mode, the Raman spectrum of each point was acquired in static mode (fixed at 1150 cm^{-1}) for 1 × 1 s running time. To obtain a good estimate of the Raman spectral parameter (Sforna et al., 2014), at least 20 points were measured on each microfossil or AOM. Recorded spectral data were processed with the software "Renishaw Wire 4.1". Out of a total of 1220 spectra acquired, only 914 have been considered (Table 1, Fig. 3). Indeed, some spectra showed a lower resolution due to signal noise and intense fluorescence. To obtain a good estimate for calculated ratios, we excluded these spectra. The baseline subtraction protocol was performed on a truncated spectrum between 1000 and 1800 cm^{-1}. The baseline was subtracted with a third order polynomial fit that was generated using the 'Through chosen points on each spectrum' mode of Wire 4.1 and was constrained by placing anchoring lines each 10 cm^{-1} between 1000 and 1100 cm^{-1} and between 1720 and 1800 cm^{-1}. Following this data processing, D1-, D2-, D3-, D4- and G-bands (Fig. 2 and Fig. A3) were fitted by a decomposition based on Gaussian–Lorentzian function with the protocol described in Sforna et al. (2014). This allowed retrieving the position, intensity, area and width of D1-, D2-, D3-, D4- and G-bands (Figs. 2, 3 and Fig. A3).

4.2. Solid bitumen reflectance

Only samples from Congo Basin were analyzed (Fig. A4) due to a privacy policies for Taoudeni and Officer samples. Analyses were performed at RWTH Aachen University (Rheinisch-Westfälische Technische Hochschule Aachen). Laboratory protocol matches the guidelines set out in the International Organization for Standardization publications ISO 7404-2, ISO 7404-3 and ISO 7404-5 and in Taylor et al. (1998). Details of sample preparation are described in Sachse et al. (2012). Solid bitumen reflectance measurements were performed on polished core sections under reflected light using a Zeiss microphotometric system, which was calibrated by a Zeiss yttrium–aluminum–garnet standard (R — 0.889%). The photometer was provided with a pinhole aperture to read a spot with a diameter of 5 μm on the sample surface at a wavelength of 546 nm, using a 50 ×/1.00 n.a. lens in oil immersion (n_e — 1.518). To reach sufficient accuracy of solid bitumen measurements, at least 30 point measurements were taken per polished section. Data processing was performed with Diskus Fossil software (*Technisches Büro, Carl H. Hilgers*).

4.3. Mineralogical analysis and Kübler index (KI)

Mineralogical compositions and clay minerals (Figs. A6, A7 and A8) were determined by X-ray diffraction (XRD) at the University of Liège (AGEs laboratory, UR GEOLOGY, Belgium). For mineralogical composition, 1 g of fresh sample (total rock) was crushed and sieved to 150 μm size particles, installed on a sample holder and then compacted carefully and regularly in order to limit any preferential orientation of minerals (Moore and Reynolds, 1997). The XRD was then performed on a Bruker AXS D8 Advance Eco diffractometer (Cu-Kα radiation, 40 kV and 25 mA), equipped with a linear detector (LINXEYE XE) for the angles between 2 and 70 Δ°2θ, with a step size of 0.02 Δ°2θ. Minerals were first identified using EVA 3.2 software and quantified with Topas (software using the Rietveld method).

In order to identify clay minerals, oriented aggregates (Moore and Reynolds, 1997) were prepared from < 2 μm fraction. This fraction was obtained by decantation from a suspension in distilled water (settling time calculated according to Stoke's law), of 1–2 g of dried bulk sediment previously sieved at 63 μm. For each sample, three X-ray patterns were recorded (Fig. A8): Air-dried (AD), after solvation with ethylene glycol for 24 h (EG) and after heating at 500 °C (H).

The KI values were calibrated to Kübler's original scale. Measurements were made on the EG pattern (Fig. A8) after fitting and deconvolution of three respective peaks (illite, mixed-layers and chlorite, Fig. A5) using Gaussian–Lorentzian function. Clay spectra were deconvoluted with 'Renishaw Wire 4.1' software and executed under the same process as Raman spectral analysis, with the exception that spectra were truncated between 5 and 11Δ°2θ Cu Kα. KI errors are ± 0.06°.

5. Results and discussion

5.1. Thermal Alteration Index

Microfossils from Kanshi sample (KN23–123) have color ranging from medium dark brown to dark-very dark brown corresponding to a TAI scale of 3 to 3^+ (Figs. 4 & A2). The microfossils from Lubi (LU18–312) have a TAI of $3^+/4^-$ as their colors range from dark- very dark brown to very dark brown-black. The CM contained in the Congo samples is thus mature to post-mature and corresponds to a burial temperature between 150 °C and 250 °C. The samples from the three Taoudeni Basin drill cores display acritarchs with wall color ranging from yellow-orange to orange-orange brown for S2–216 sample, and medium dark brown in S3–123 and S4–162 samples. This correspond to TAI values of $2/2^+$, and 3, respectively. The CM preserved in the Taoudeni samples is thus immature in S2 and mature for S3 and S4 and has registered a burial temperature < 60 °C and between 90 and 200 °C, respectively. Acritarchs from the three samples (L1–472; L1–680 and L1–955) of the Officer Basin show wall color ranging from medium light brown to medium dark brown corresponding to a TAI scale of 3^- to 3 (Fig. 4). These TAI values correspond to mature CM and temperatures of burial < 100 °C (Al-Ameri and Wicander, 2008).

5.2. Kübler index

Shale samples are mainly characterized by illite, kaolinite, chlorite and a few percent of mixed-layers (illite-vermiculite), and non-clay minerals such as quartz, feldspar and minor phases such as pyrite, carbonate (except sample S2) and gypsum (Fig. A6). In EG spectra, after deconvolution (Fig. A5), excluding the 6.35°2θ chlorite peak, two elementary peaks occur between 5 and 11°2θ. A peak at ca. 8.8°2θ is attributed to illite, whereas a wider peak at 8.5°2θ corresponds to 10–14 mixed layers, interpreted as illite-vermiculite. In the Congo Basin samples, the KI values range from 0.57 to 0.82 Δ°2θ (KN23–123: 0.82, LU18–312: 0.57, Fig. A5, Table 2). In the Taoudeni Basin samples, the KI values vary between 0.48 and 1.98 Δ°2θ (S4–162: 0.48; S3–123: 0.98; S2: 1.48). Finally, in the Officer Basin samples, the KI values show also similar values ranging from 0.87 to 1.23 Δ°2θ (L1–472: 1.23; L1–680: 0.87). All these data suggest that temperatures undergone by the samples are < 200 °C and in the diagenesis domain (Fig. 4). The diagenetic origin of fibrous illite is confirmed by the study of *Hamilton (in*Mory and Haines, 2005) in clays from the Kanpa Formation within the Lancer1 drill core (Officer Basin, Australia). This is also supported by a large content of kaolinite in our samples (until 20%, Fig. A6), indicating temperatures lower than 200 °C (Cathelineau et al., 1985).

5.3. Raman spectra and characteristic spectral parameters

Representative spectra from microfossil species and AOM for each sample are shown in Fig. 2. Spectral parameters are displayed in Fig. 3, Table 1 and in Table A. For each of our studied samples from three different basins, the Raman spectra and the spectral parameters for extracted kerogen and thin section within one sample are similar (Fig. 2), even if the spectra acquired on thin section are noisier due to the intrinsic fluorescence of the matrix. AOM and microfossils spectra (Fig. 2) display well-developed D3- and D4-bands, have a D2-band unseparated from the G-band, a broad D1-band (FWHM-D1 > 100 cm^{-1}) and an intensity ratio I_{D1}/I_G lower than 1. These characteristics are typical of spectra of poorly ordered CM (Beyssac et al., 2002, 2003; Kouketsu et al., 2014; Lahfid et al., 2010; Sauerer et al., 2017).

There is no significant difference in the band positions between spectra acquired on extracted kerogen or on thin section for a given

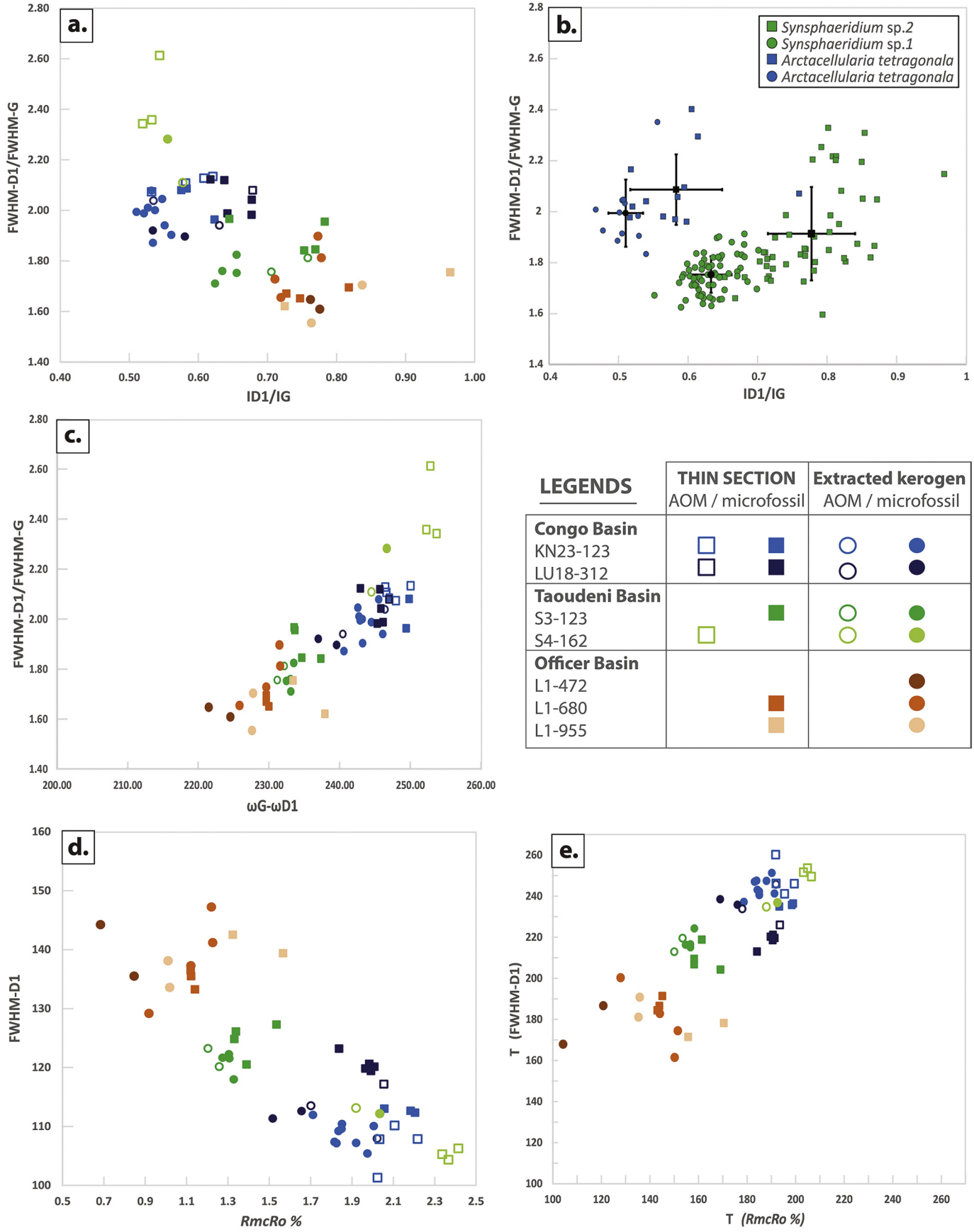

Fig. 3. (a) Average values of FWHM-D1/FWHM-G ratio vs ID1/IG ratio. (b) Analyses for the specimens Synsphaeridium in S3 drill core and Arctacellularia tetragonala in Kanshi drill core (extracted kerogen and thin section). Means and standard deviations are in black. (c) FWHM-D1/FWHM-G ratio vs ωG-ωD1. (d) FWHM-D1 vs $RmcR_o$% and (e) T FWHM-D1 (Eq. 5) and T $RmcR_o$%.

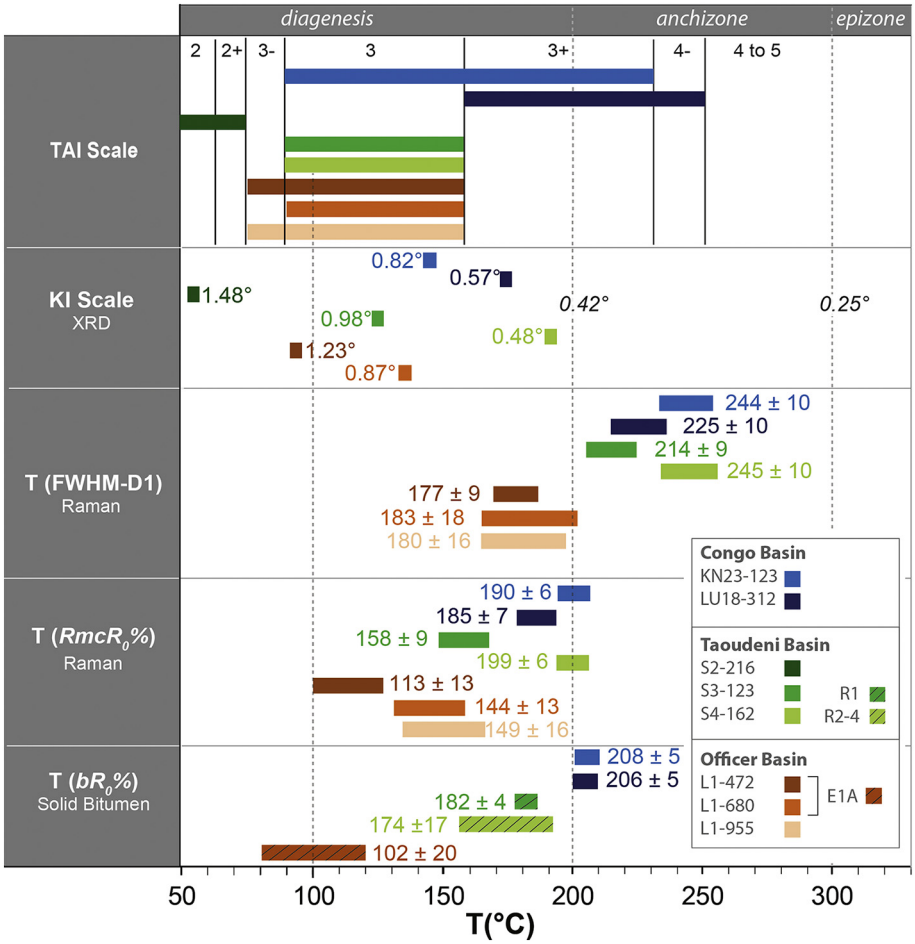

Fig. 4. Compilation of all thermometers used in this study and corresponding mean temperature range. All data come from Table 2. Errors are given in 1σ. Data from dashed boxes are from Martín-Monge et al. (2017) and Ghori (in Stevens and Apak, 1999).

microfossil species (Tables 1 and 2). For example, within spectra acquired on a specimen of *Arctacellularia tetragonala* isolated from extracted kerogen and other specimen within a thin section, the average position of D1- band are 1350 cm^{-1} and 1351 cm^{-1}, respectively. As for the average positions of G-band, they are 1593 cm^{-1} and 1598 cm^{-1}, respectively (Table 1). There is a slight shift towards lower values for the width and the intensity of the different bands for microfossils from extracted kerogen (Fig. 3b, Table 2 and Table A). These shifts are limited and comprised within two σ range. The dispersion of the data is systematically larger for the thin sections compared to the extracted kerogen whatever the drill core or the microfossil considered (Fig. 3b, Table 2 and Table A). For example, the standard deviation (1σ) on the I_{D1}/I_G ratio for *Arctacellularia tetragonala* is divided by 3 (thin section: 0.07, extracted kerogen: 0.02, Fig. 3b, Table 1) while it is divided by 2 for *Synsphaeridium* (thin section: 0.06, extracted kerogen: 0.03, Fig. 3b, Table 1). For the FWHM-D1/FWHM-G, the value for *Synsphaeridium* is divided by 2 (thin section: 0.17, extracted kerogen: 0.07, Fig. 3b, Table 1) while the values do not change between extracted kerogen and thin section for *Arctacellularia tetragonala*. This is related to high sensitivity of I_{D1}/I_G to peak fitting and baseline subtraction procedures whereas FWHM-D1/FWHM-G is less sensitive (Beyssac et al., 2003; Kouketsu et al., 2014).

The small differences within the spectra and spectral parameters observed from a species to another species and with the AOM could be explained by a difference in the CM precursors. Despite these minor differences, the uniformity of the Raman spectra and spectral parameters show that microfossils and AOM registered, here, the same thermal history. It often occurs that AOM can be remobilized or inherited, so it is best to make measurement on microfossils for which syngenicity can be evidenced by their distribution in shale: flattened parallel to bedding. The smaller dispersion of data for extracted kerogen leads to better estimates of calculated ratios and thus of the maturity and calculated temperatures. This should be particularly true for low maturity CM that displays high intrinsic fluorescence (Quirico et al., 2005).

D1-band position (ωD1, Tables 1 and Table A) has average values of ~1356 cm^{-1} (L1), ~1354 cm^{-1} (S3–123), ~1352 cm^{-1} (LU18–312), ~1349 cm^{-1} (KN23–123 and S4–162). Conversely, the G-band position (ωG) increases towards higher frequencies with values of ~1580 cm^{-1} (L1–472), ~1584 cm^{-1} (L1–680), ~1587 cm^{-1} (L1–955 and S3–123: ~1587 cm^{-1}), ~1595 cm^{-1} (LU18–312 and KN23–123) and ~1599 cm^{-1} (S4–162). As a consequence, the ωG-ωD1 difference increases (Fig. 3c; Table 1 and Table A), from ~230 cm^{-1} for Lancer samples to ~250 cm^{-1} for S4. FWHM-D1 and FWHM-G are the highest for Lancer samples (FWHM-D1 ~ 138 cm^{-1} and FWHM-G ~ 82 cm^{-1}) and the lowest for S4 (FWHM-D1 ~ 108 cm^{-1} and FWHM-G ~ 47 cm^{-1}). The FWHM-D1/FWHM-G ratio is correlated positively with the ωG-ωD1difference (R^2 = 0.594; Fig. 3c) but negatively with the ID1/IG ratio (R^2 = 0.48; Fig. 3a). The evolution of these parameters and these ratios are coherent with an increasing order of the CM and thus a rise of the maturity degree (Beyssac et al., 2002; Liu et al., 2013; Sauerer et al., 2017).

5.4. Raman and solid bitumen reflectance

Raman reflectance derives directly from the ωG-ωD1 difference measured on the Raman spectrum. The full fitting protocol used in this study is difficult to apply when the CM is highly immature (i.e. highly disordered) due to its high fluorescence. As the position of D1- and G-band are almost not sensible to the fitting procedure (Beyssac et al., 2003; Kouketsu et al., 2014), we retrieved, for 30 acquisitions made on one *Synsphaeridium* specimen from Congo (Table B), the positions of D1- and G-bands after application of the full fitting protocol and by directly reading them on the Raman spectra. After calculating the ωG-ωD1 difference with the two extraction protocols, the $RmcR_0$% is the same (Table B). This suggests that for highly immature CM, the Raman Reflectance method is efficient to obtain a good equivalent of the vitrinite reflectance. Values of $RmcR_0$% are presented in Fig. 3e, Tables 1 and 2. Within the same sample, the results are lower for extracted kerogen than in thin section. For example, $RmcR_0$% calculated for KN23–123 ranges in the 1.71–2.02% interval for extracted kerogen while it ranges between 2.02 and 2.22% in thin section. A similar shift of 0.1–0.4% can be observed for all the samples (Tables 1 and 2). However, these $RmcR_0$% values still correspond to the same range of vitrinite reflectance equivalence and thus are not in strong disagreement (Liu et al., 2013). The calculated $RmcR_0$% increases from 0.96 ± 0.18% for Lancer, to 1.27 ± 0.13% for S3–123, 1.64 ± 0.15% for LU18–312, 1.87 ± 0.15% for KN23–123 and 1.97 ± 0.14% for S4–162 (Table 2 and Fig. 3d), suggesting an increase of CM thermal maturity for these samples studied.

Solid bitumen of KN23–123 and LU18–312 samples from Congo Basin occurs as an opaque material of greyish appearance, disseminated in pores and fissures (Fig. A3). Solid bitumen in these samples is either homogeneous, locally elongated and filling fissures or granular. Reflectance histograms of KN23–123 and LU18–312 exhibit a near uniform distribution with bR_0% mean values of 2.28 ± 0.16% and 2.22 ± 0.15%, respectively (Table 2 and Fig. A4). The vR_0eq % obtained from bR_0% ranges from 2.23 to 2.78% and 2.09 to 2.64% for KN23–123 and LU18–312, respectively (Table C). These vR_0eq % are systemically higher than the $RmcR_0$% of ~0.6% (Table 2).

The $RmcR_0$% we obtained for S3 and S4 samples can be compared to the vR_0eq % measured from methylphenanthrene index (Martín-Monge et al., 2017) within the R1 well, equivalent to S3, and within the R2–4 wells, equivalent to S4 drill core (Martín-Monge et al., 2017). Interestingly, the $RmcR_0$% values for S3 (1.20–1.33%) are lower than the vR_0eq % for R1 well (1.72–1.85%; Martín-Monge et al., 2017) while the $RmcR_0$% values for S4 (1.92–2.03%) are higher than the R2–4 wells mean vR_0eq % values (1.17–2.04%, μ = 1.65%; Martín-Monge et al., 2017). These differences could be attributed to a difference in the nature of the CM analyzed or their precursors to obtain these equivalents of vitrinite reflectance (kerogen, solid bitumen, methylphenanthrene index). However, when the maturity degree is considered, the two vR_0eq % fall in the same maturity range (Liu et al., 2013) and can thus be considered equivalent. No data was available for Lancer 1 drill core. However, vR_0eq % obtained from fluorescent lamalginite were reported in the Kanpa Formation within Empress 1A drill core (*Ghori in*Stevens and Apak, 1999). Samples from 516.6 to 830.3 m-depth, equivalent to our Lancer 1 samples, have vR_0eq values between 0.52 and 1.00%. These values are in the same range than our $RmcR_0$% for Lancer 1 (0.76–1.01%). These results indicate that Raman reflectance is a fast, robust and non-destructive tool to evaluate the thermal maturity of carbonaceous material and in particular Proterozoic materials, especially if they are at low maturity levels.

5.5. Raman geothermometry

Raman spectra and characteristic ratios, as well as $RmcR_0$% values all show a similar evolution of the thermal maturity of the CM contained in samples from the Congo, Taoudeni and Officer basins (Fig. 4). There is a progressive increase of thermal maturity from the S2–216 sample to the Lancer 1 samples (L1–472 < L1–680 < L1 955), the S3 sample (S3–123), the Congo samples (LU18–312 ≤ KN23–123) and finally the S4 sample (S4–162). This increasing order of maturity is confirmed with the increasing range of temperature estimates.

Temperatures calculated with Kouketsu geothermometer (T(FWHM-D1); Eq. 1) and Raman reflectance (T($RmcR_0$%); Eq. 3) are summarized in Figs. 3e, 4 and in Tables 1, 2. Mean temperatures from Kouketsu geothermometer are ranging from 177 to 245 °C (L1–472: 177 ± 9 °C; L1–955: 180 ± 16 °C; L1–680: 183 ± 18 °C; S3–123: 214 ± 9 °C; LU18–312: 225 ± 10 °C; KN23–123: 244 ± 10 °C and S4–162: 245 ± 10 °C). Mean temperatures from $RmcR_0$% (T $RmcR_0$%) also reflect the same trend, with a range between 113 and 199 °C (L1–472: 113 ± 13 °C; L1–680: 144 ± 13 °C; L1–955: 149 ± 16 °C; S3–123: 158 ± 9 °C; LU18–312: 185 ± 7 °C; KN23–123: 190 ± 6 °C and S4–162: 199 ± 6 °C).

FWHM-D1 and $RmcR_0$% are correlated (R^2 = 0.643, Fig. 3e); as a consequence, the two Raman-based thermometers show the same order of temperature increase (Fig. 3d,e). Nonetheless, T(FWHM-D1) are always ~50 °C higher than the T($RmcR_0$%) (Fig. 3e, 4). However, Kouketsu et al. (2014) gave an empirical error for their thermometer of ± 30 °C. Taking into account this error, the temperature estimate obtained with this thermometer could enter within the diagenesis domain. This suggests that the temperature achieved in the three basins lies certainly in between the two obtained temperature ranges.

5.6. Comparison of methods

As summarize in Fig. 4, Kübler index show that all studied samples have been known a thermal evolution restricted to diagenesis domain, i.e. < 200 °C (Kübler, 1967). This is also confirmed by TAI scale values with the exception of samples from Congo Basin for which values extend beyond diagenesis domain (i.e. up to 250 °C). The temperatures obtained from solid bitumen reflectance, for samples from Congo basin, are ca. 207 °C and correspond to the upper range of the T($RmcR_0$%). For samples from Officer and Taoudeni basins, literature data of vitrinite equivalent (vR_0eq %) from methylphenanthrene index (Martín-Monge et al., 2017) and lamalginite (*Ghori in*Stevens and Apak, 1999), respectively, give also temperatures which are in accordance with the diagenesis domain. Overall, whatever the nature of carbonaceous material (solid bitumen, methylphenanthrene or lamalginite), T(vR_0eq %) are consistent with temperatures from Raman Reflectance T($RmcR_0$%). TAI scale and Kübler index from these different Proterozoic sequences are also compatible with T($RmcR_0$%). By contrast, T(FWHM-D1) give temperatures higher than those of the diagenesis domain for Congo and Taoudeni samples. For Officer samples, T(FWHM-D1) falls into the diagenesis domain with an overestimate of ~50 °C. Relative to conventional techniques cited above, results from T($RmcR_0$%) seem more consistent than those from T(FWHM-D1). However, with the possibility of being measured directly on any unambiguous microfossils, Raman Reflectance excludes the risk of disturbance by inherited minerals which restricts sometime the use of Kübler index (Kübler, 1967). In addition, Raman reflectance is more accurate than the subjective TAI (see Section 3.1 above) and also probably easier to use than solid bitumen reflectance, for which only a homogeneous variety is recommended for thermal history studies (see Section 3.3 above). The Raman reflectance thus appears to be a valuable tool to evaluate the thermal maturity of poorly ordered carbonaceous material at various stages of diagenesis.

6. Conclusions

Raman spectra measured on microfossils and amorphous organic matter in both extracted kerogen and in situ in thin sections allowed to evaluate the thermal maturity of samples from the three studied Proterozoic sedimentary sequences. We obtain estimates temperatures

by using Raman Kouketsu geothermometry, reflectance geothermometers (Raman reflectance and solid bitumen reflectance), illite crystallinity and Thermal Alteration Index. All these techniques provide consistent range of temperatures except for Raman Kouketsu geothermometry, which gives slightly higher estimates. The consistency of results from one method to another validates the use of Raman reflectance as a robust tool to evaluate the thermal maturity of poorly-organized (disordered) carbonaceous material from Proterozoic rocks. This technique is well suited at low temperatures (< 300 °C). We also demonstrate that extracted kerogen provides accurate estimates for thermal maturity relative to kerogen in thin section. Thus, our study shows that the rapid and non-destructive Raman measurements on dispersed kerogenous material (microfossils and amorphous organic matter) could be used successfully to quantify the thermal evolution of a sedimentary succession.

Supplementary data to this article can be found online at https://doi.org/10.1016/j.coal.2018.03.007.

Acknowledgements

The authors are grateful to K. Grey (Geological Survey of West Australia, Perth, Australia) for access of the Lancer 1 drill core; to JP Houzay, C. Blanpied and Total S.A. (TOTAL Projets Nouveaux, Paris, France), for access to the S2 drill core; to J. J. Brocks (The Australian National University, Canberra, Australia) and S. W. Poulton (University of Leeds, Leeds, United Kingdom) for access to the samples of the S3 and S4 drill cores; and to The Royal Museum for Central Africa (Tervuren, Belgium) for access to the Kanshi S13B and Lubi drill cores. We also thank D. Macherey for sample preparation and for help during solid bitumen reflectance measurements (RWTH Aachen University, Germany), M. Giraldo and J. Laval (University of Liège, Geology Department, Belgium) for sample preparation and E. Pleuger (University of Liège, UR Geology, Belgium) for help during XRD analyses. This work was supported by the European Research Council Stg ELITE FP7/308074 to B.K.B., Y.C., J.-Y.S., E.J.J. (P.I.); the BELSPO IAP PLANET TOPERS to CF, JB, E.J.J. (PI), and the Marie-Curie Cofund program at the University of Liège to M.C.S.

References

Al-Ameri, T., Wicander, R., 2008. An assessment of the gas generation potential of the Ordovician Khabour Formation, Western Iraq. Comun. Geol. 95, 157–166.

Albert-Villanueva, E., Permanyer, A., Tritlla, J., Levresse, G., Salas, R., 2016. Solid hydrocarbons in proterozoic dolomites, taoudeni basin, Mauritania. J. Pet. Geol. 39, 5–27. http://dx.doi.org/10.1111/jpg.12625.

Baludikay, B.K., Storme, J.-Y., Francois, C., Baudet, D., Javaux, E.J., 2016. A diverse and exquisitely preserved organic-walled microfossil assemblage from the Meso-Neoproterozoic Mbuji-Mayi Supergroup (Democratic Republic of Congo) and implications for Proterozoic biostratigraphy. Precambrian Res. 281, 166–184. http://dx.doi.org/10.1016/j.precamres.2016.05.017.

Barker, C.E., Pawlewicz, M.J., 1994. Calculation of vitrinite reflectance from thermal histories and peak temperatures. a comparison of methods. ACS Symp. Ser. 570, 216–229.

Begg, G.C., Griffin, W.L., Natapov, L.M., O'Reilly, S.Y., Grand, S.P., O'Neill, C.J., Hronsky, J.M.A., Djomani, Y.P., Swain, C.J., Deen, T., Bowden, P., 2009. The lithospheric architecture of Africa: seismic tomography, mantle petrology, and tectonic evolution The lithospheric architecture of Africa. Geosphere 5, 23–50.

Beghin, J., Storme, J.-Y., Blanpied, C., Gueneli, N., Brocks, J.J., Poulton, S.W., Javaux, E.J., 2017. Microfossils from the late Mesoproterozoic – early Neoproterozoic Atar/El Mreïti Group, Taoudeni Basin, Mauritania, northwestern Africa. Precambrian Res. 291, 63–82. http://dx.doi.org/10.1016/j.precamres.2017.01.009.

Bertrand, R., 1990. Correlations among the reflectances of vitrinite, chitinozoans, graptolites and scolecodonts. Org. Geochem. 15, 565–574.

Bertrand, R., Héroux, Y., 1987. Chitinozoan, graptolite, and scolecodont reflectance as an alternative to vitrinite and pyrobitumen reflectance in Ordovician and Silurian strata, Anticosti Island, Quebec, Canada. Am. Assoc. Pet. Geol. Bull. 71, 951–957.

Beyssac, O., Goffé, B., Chopin, C., Rouzaud, J.N., 2002. Raman spectra of carbonaceous material in metasediments: a new geothermometer. J. Metamorph. Geol. 20, 859–871. http://dx.doi.org/10.1046/j.1525-1314.2002.00408.x.

Beyssac, O., Goffé, B., Petitet, J.P., Froigneux, E., Moreau, M., Rouzaud, J.N., 2003. On the characterization of disordered and heterogeneous carbonaceous materials by Raman spectroscopy. Spectrochim. Acta A Mol. Biomol. Spectrosc. 59, 2267–2276. http://dx.doi.org/10.1016/S1386-1425(03)00070-2.

Cahen, L., Snelling, N.J., Delhal, J., Vail, J.R., Bonhomme, M., Ledent, D., 1984. The Geochronology and Evolution of Equatorial Africa. Clarendon, Oxford, pp. 512.

Camacho, A., Armstrong, R., Davis, D.W., Bekker, A., 2015. Early history of the Amadeus Basin: implications for the existence and geometry of the Centralian Superbasin. Precambrian Res. 259, 232–242. http://dx.doi.org/10.1016/j.precamres.2014.12.004.

Cathelineau, M., Olivier, R., Nieva, D., Garfias, A., 1985. Mineralogy and distribution of hydrothermal mineral zones in Los Azufres (Mexico) geothermal field. Geothermics 14, 49–57.

Cotter, K.L., 1997. Neoproterozoic microfossils from the Officer Basin, Western Australia. Alcheringa 21, 247–270. http://dx.doi.org/10.1080/03115519708619166.

Delpomdor, F., Blanpied, C., Virgone, A., Préat, A., 2015. Sedimentology and sequence stratigraphy of the late precambrian carbonates of the mbuji-mayi supergroup in the sankuru-mbuji-mayi-lomami- lovoy basin (Democratic Republic of the Congo). In: De Wit, M.J., Guillocheau, F., De Wit, M.C.J. (Eds.), Geology and Resource Potential of the Congo Basin. Springer-Verlag, Berlin Heidelberg, pp. 59–76. http://dx.doi.org/10.1007/978-3-642-29482-2.

Delpomdor, F., Bonneville, S., Baert, K., Préat, A., 2018. An introduction to the Precambrian petroleum system in the Sankuru–Mbuji-May–Lomami–Lovoy Basin, South-Central Democratic Republic of Congo. J. Pet. Geol. 41 (I), 5–27.

Delvaux, D., Barth, A., 2010. African stress pattern from formal inversion of focal mechanism data. Tectonophysics 482, 105–128. http://dx.doi.org/10.1016/j.tecto.2009.05.009.

Delvaux, D., Fernandez, M., 2015. Petroleum potential of the congo basin. In: de Wit, M., Guillochau, F., de Wit, M.C.J. (Eds.), The Geology and Resource Potential of the Congo Basin. Regional Geology Reviews, Springer, Heidelberg, pp. 371–391. http://dx.doi.org/10.1007/978-3-642-29482-2_18.

Dippel, B., Jander, H., Heintzenberg, J., 1999. NIR FT Raman spectroscopic study of flame soot. Phys. Chem. Chem. Phys. 1, 4707–4712. http://dx.doi.org/10.1039/a904529e.

Du, J., Geng, A., Liao, Z., Cheng, B., 2014. Potential Raman parameters to assess the thermal evolution of kerogen from different pyrolysis experiments. J. Anal. Appl. Pyrolysis 107, 242–249. http://dx.doi.org/10.1016/j.jaap.2014.03.007.

Dunoyer de Segonzac, G., 1969. Les minéraux argileux dans la diagenèse — passage au métamorphisme. Mém. Serv. Carte Géol. Als-Lorr. 29, 1–320.

Espitalié, J., Laporte, J.L., Madec, M., Marquis, F., Leplat, P., Paulet, J., Boutefeu, A., 1977. Méthode rapide de caracterisation des roches mères, de leur potential petrolier et de leur degré d'évolution. Revue de l'Institut français du Pétrole 32, 23–42.

Ferrari, A.C., Robertson, J., 2000. Interpretation of Raman spectra of disordered and amorphous carbon. Phys. Rev. B 61, 14095–14107. http://dx.doi.org/10.1103/PhysRevB.61.14095.

Ferreiro Mählmann, R., Frey, M., 2012. Standardisation, calibration and correlation of the Kübler-index and the vitrinite/bituminite reflectance: an inter-laboratory and field related study. Swiss J. Geosci. 105, 153–170.

Ferreiro Mählmann, R., Bozkaya, Ö., Potel, S., Le Bayon, R., Šegvić, B., Nieto, F., 2012. The pioneer work of Bernard Kübler and Martin Frey in very low-grade metamorphic terranes: paleo-geothermal potential of variation in Kübler-index/organic matter reflectance correlations. A review. Swiss J. Geosci. 105, 121–152.

François, C., Baludikay, B.K., Storme, J.-Y., Baudet, D., Paquette, J.L., Fialin, M., Javaux, E.J., 2017. Contributions of U-Th-Pb dating on the diagenesis and sediment sources of the lower group (BI) of the Mbuji-Mayi Supergroup (Democratic Republic of Congo). Precambrian Res. 298, 202–219. http://dx.doi.org/10.1016/j.precamres.2017.06.012.

Grey, K., 1999. A modified palynological preparation technique for the extraction of large Neoproterozoic acanthomorph acritarchs and other acid-insoluble microfossils. In: Western Australia Geological Survey, Record 1999/10, pp. 23.

Grey, K., Hill, A.C., Calver, C., 2011. Chapter 8 Biostratigraphy and stratigraphic subdivision of Cryogenian successions of Australia in a global context. Geol. Soc. Lond. Mem. 36, 113–134.

Guggenheim, S., Bain, D.C., Bergaya, F., Brigatti, M.F., Drits, V.A., Eberl, D.D., Formoso, M.L.L., Galán, E., Merriman, R.J., Peacor, D.R., Stanjek, H., Watanabe, T., 2002. Report of the Association Internationale pour L'étude des Argiles (AIPEA) Nomenclature Committee for 2001: Order, disorder and crystallinity in phyllosilicates and the use of the "crystallinity index". Clay Clay Miner. 50, 406–409. http://dx.doi.org/10.1346/000986002760833783.

Hartkopf-Fröder, C., Königshof, P., Littke, R., Schwarzbauer, J., 2015. Optical thermal maturity parameters and organic geochemical alteration at low grade diagenesis to anchimetamorphism: a review. Int. J. Coal Geol. 150-151, 74–119.

Jaboyedoff, M., Kübler, B., Sartori, M., Thélin, P., 2000. Basis for meaningful illite crystallinity measurements: an example from the Swiss Prealps. Bull. suisse Minér. Pétrogr. 80, 75–83.

Jaboyedoff, M., Bussy, F., Kübler, B., Thélin, P., 2001. Illite crystallinity revisited. Clay Clay Miner. 49 (2), 156–167.

Jacob, H., 1989. Classification, structure, genesis and practical importance of natural solid oil bitumen ("migrabitumen"). Int. J. Coal Geol. 11, 65–79. http://dx.doi.org/10.1016/0166-5162(89)90113-4.

Jasper, K., Krooss, B.M., Flajs, G., Hartkopf-Fröder, C., Littke, R., 2009. Characteristics of type III kerogen in coal-bearing strata from the Pennsylvanian (Upper Carboniferous) in the Ruhr Basin, Western Germany: comparison of coals, dispersed organic matter, kerogen concentrates ans coal-mineral mixtures. Int. J. Coal Geol. 80, 1–19.

Javaux, E.J., Marshall, C.P., Bekker, A., 2010. Organic-walled microfossils in 3.2-billion-year-old shallow-marine siliciclastic deposits. Nature 463, 934–938.

Kadima, E., Delvaux, D., Sebagenzi, S.N., Tack, L., Kabeya, M., 2011a. Structure and geological history of the Congo Basin: an integrated interpretation of gravity, magnetic and reflection seismic data. Basin Res. 23 (5), 499–527. http://dx.doi.org/10.1111/j.1365-2117.2011.00500.x.

Kadima, E.K., Sebagenzi, S.M.N., Lucazeau, F., 2011b. A Proterozoic-rift origin for the

structure and evolution of the cratonic Congo Basin. Earth Planet. Sci. Lett. 304, 240–250. http://dx.doi.org/10.1016/j.epsl.2011.01.037.
Kouketsu, Y., Mizukami, T., Mori, H., Endo, S., Aoya, M., Hara, H., Nakamura, D., Wallis, S., 2014. A new approach to develop the Raman carbonaceous material geothermometer for low-grade metamorphism using peak width. Island Arc 23, 33–50. http://dx.doi.org/10.1111/iar.12057.
Kübler, B., 1964. Les argiles, indicateurs de métamorphisme. 19. Revue de l'Institut Francaise du Petrole, pp. 1093–1112.
Kübler, B., 1967. La cristallinité de l'illite et les zones tout à fait supérieures du métamorphisme. In: Etages tectoniques-Colloques Neuchâtel, 18–21 Avril 1967, pp. 105–122.
Kübler, B., Jaboyedoff, M., 2000. Illite crystallinity. Comptes Rendus l'Académie Sci. - Ser. IIa Sci. la Terre des Planétes 331, 75–89.
Lahfid, A., Beyssac, O., Deville, E., Negro, F., Chopin, C., Goffé, B., 2010. Evolution of the Raman spectrum of carbonaceous material in low-grade metasediments of the Glarus Alps (Switzerland). Terra Nova 22, 354–360. http://dx.doi.org/10.1111/j.1365-3121.2010.00956.x.
Lahondère, D., Thiéblemont, D., Goujou, J.C., Roger, J., Moussine-Pouchkine, A., Le Métour, J., Cocherie, A., Guerrot, C., 2003. Notice explicative des cartes géologiques et gîtologiques à 1/200 000 et 1/500 000 du nord de la Mauritanie. Vol. 1.
Landis, C.R., Castaño, J.R., 1995. Maturation and bulk chemical properties of a suite of solid hydrocarbons. Org. Geochem. 22, 137–149. http://dx.doi.org/10.1016/0146-6380(95)90013-6.
Littke, R., Urai, J.L., Uffmann, A.K., Risvanis, F., 2012. Reflectance of dispersed vitrinite in Palaeozoic rocks with and without cleavage: implications for burial and thermal history modeling in the Devonian of Rursee area, northern Rhenish Massif, Germany. Int. J. Coal Geol. 89, 41–50.
Liu, D.H., Xiao, X.M., Tian, H., Min, Y.S., Zhou, Q., Cheng, P., Shen, J.G., 2013. Sample maturation calculated using Raman spectroscopic parameters for solid organics: methodology and geological applications. Chin. Sci. Bull. 58, 1285–1298. http://dx.doi.org/10.1007/s11434-012-5535-y.
Lucazeau, F., Armitage, J., Kadima Kabongo, E., 2015. Thermal Regime and Evolution of the Congo Basin as an Intracratonic Basin. In: De Wit, M.J., Guillocheau, F., De Wit, M.C.J. (Eds.), Geology and Resource Potential of the Congo Basin. Springer-Verlag, Berlin Heidelberg, pp. 229–244. http://dx.doi.org/10.1007/978-3-642-29482-12.
Lünsdorf, N.K., Dunkl, I., Schmidt, B.C., Rantitsch, G., von Eynatten, H., 2014. Towards a higher comparability of geothermometric data obtained by Raman spectroscopy of carbonaceous material. Part 1: evaluation of biasing factors. Geostand. Geoanal. Res. 38 (1), 73–94.
Marshall, C.P., Javaux, E.J., Knoll, A.H., Walter, M.R., 2005. Combined micro-Fourier transform infrared (FTIR) spectroscopy and micro-Raman spectroscopy of Proterozoic acritarchs: a new approach to Palaeobiology. Precambrian Res. 138, 208–224. http://dx.doi.org/10.1016/j.precamres.2005.05.006.
Martín-Monge, A., Baudino, R., Gairifo-Ferreira, L.M., Tocco, R., Badali, M., Soriano, S., El Hafiz, N., Hernán-Gómez, J., Chacón, B., Brisson, I., Grammatico, G., Varadé, R., Abdallah, H., 2017. An Unusual Proterozoic Petroleum Play in Western Africa: The Atar Group Carbonates (Taoudeni Basin, Mauritania). 438 Geological Society - Special Publications (39pp). https://doi.org/10.1144/SP438.5.
Moore, D.M., Reynolds, R.C., 1997. X-Ray Diffraction and the Identification and Analysis of Clay Minerals, 2nd ed. Oxford University Press, Oxford, New York.
Mory, A., Haines, P., 2005. Gswa Lancer 1 Well Completion Report (Interpretive Papers) Officer and Gunbarrel Basins Western Australia. In: Geological Survey of Western Australia, Theatre Record 2005/4, pp. 90.
Nemanich, R.J., Solin, S.A., 1979. First- and second-order Raman scattering from finite-sized crystals of graphite. Phys. Rev. B 20, 392–401.
Pasteris, J.D., Wopenka, B., 2003. Necessary, but not sufficient: Raman identification of disordered carbon as a signature of ancient life. Astrobiology 3, 727–738. http://dx.doi.org/10.1089/153110703322736051.
Peters, K.E., 1986. Guidelines for evaluating petroleum source rock using programmed pyrolysis. Am. Assoc. Pet. Geol. Bull. 70, 318–329.
Peters, K.E., Cassa, M.R., 1994. Applied source rock geochemistry. In: Magoon, L.B., Dow, W.G. (Eds.), The Petroleum System–from Source to Trap: AAPG Memoir. 60. pp. 93–120.
Quirico, E., Rouzaud, J.N., Bonal, L., Montagnac, G., 2005. Maturation grade of coals as revealed by Raman spectroscopy: progress and problems. Spectrochim. Acta - Part A Mol. Biomol. Spectrosc. 61, 2368–2377. http://dx.doi.org/10.1016/j.saa.2005.02.015.
Radke, M., Welte, D.H., 1983. The Methylphenanthrene Index (MPI): a maturity parameter based on aromatic hydrocarbons. In: Bjorøy, M. (Ed.), Advances in Organic Geochemistry. Wiley, Chichester, pp. 504–512.
Rahl, J.M., Anderson, K.M., Brandon, M.T., Fassoulas, C., 2005. Raman spectroscopic carbonaceous material thermometry of low-grade metamorphic rocks: calibration and application to tectonic exhumation in Crete, Greece. Earth Planet. Sci. Lett. 240, 339–354. http://dx.doi.org/10.1016/j.epsl.2005.09.055.
Raucq, P., 1970. Nouvelles acquisitions sur le Système de la Bushimay. Ann. Mus. Roy. Congo belge, Tervuren (Belgique), série in-8. Sci. Géol. 69, 156.
Riediger, C.L., 1993. Solid bitumen reflectance and Rock-Eval Tmax as maturation indices: an example from the "Nordegg Member", Western Canada Sedimentary Basin. Int. J. Coal Geol. 22, 295–315. http://dx.doi.org/10.1016/0166-5162(93)90031-5.
Rooney, A.D., Selby, D., Houzay, J.P., Renne, P.R., 2010. Re-Os geochronology of a Mesoproterozoic sedimentary succession, Taoudeni basin, Mauritania: Implications for basin-wide correlations and Re-Os organic-rich sediments systematics. Earth Planet. Sci. Lett. 289, 486–496. http://dx.doi.org/10.1016/j.epsl.2009.11.039.
Sachse, V.F., Delvaux, D., Littke, R., 2012. Petrological and geochemical investigations of potential source rocks of the Central Congo Basin, Democratic Republic of Congo. Am. Assoc. Pet. Geol. Bull. 96, 245–275. http://dx.doi.org/10.1306/07121111028.
Sauerer, B., Craddock, P.R., Aljohani, M.D., Alsamadony, K.L., Abdallah, W., 2017. Fast and accurate shale maturity determination by Raman spectroscopy measurement with minimal sample preparation. Int. J. Coal Geol. http://dx.doi.org/10.1016/j.coal.2017.02.008.
Schiffbauer, J.D., Wallace, A.F., Hunter, J.L., Kowalewski, M., Bodnar, R.J., Xiao, S., 2012. Thermally-induced structural and chemical alteration of organic-walled microfossils: an experimental approach to understanding fossil preservation in metasediments. Geobiology 10, 402–423. http://dx.doi.org/10.1111/j.1472-4669.2012.00332.x.
Schoenherr, J., Littke, R., Urai, J.L., Kukla, P.A., Rawahi, Z., 2007. Polyphase thermal evolution in the Infra-Cambrian Ara Group (South Oman Salt Basin) as deduced by maturity of solid reservoir bitumen. Org. Geochem. 38, 1293–1318. http://dx.doi.org/10.1016/j.orggeochem.2007.03.010.
Sforna, M.C., van Zuilen, M.A., Philippot, P., 2014. Structural characterization by Raman hyperspectral mapping of organic carbon in the 3.46 billion-year-old Apex chert, Western Australia. Geochim. Cosmochim. Acta 124, 18–33. http://dx.doi.org/10.1016/j.gca.2013.09.031.
Staplin, F.L., 1969. Sedimentary organic matter, organic metamorphism, and oil and gas occurrence. Bull. Can. Petrol. Geol. 17, 47–66.
Staplin, F.L., 1977. Interpretation of thermal history from color of particulate organic matter: a review. Palynology 1, 9–18. http://dx.doi.org/10.2307/3687312.
Stevens, M.K., Apak, S.N., 1999. GSWA Empress 1 and 1A well completion report Yowalga Sub-basin, Officer Basin Western Australia. In: Geol. Surv. West. Aust. Rec. 1999/4, (118pp).
Szczepanik, Z., 1997. Preliminary results of thermal alteration investigations of the Cambrian acritarchs in the Holy Cross Mts. Geol. Q. 41, 257–264.
Taylor, G.H., Teichmüller, M., Davis, A., Diessel, C.F.K., Littke, R., Robert, P., 1998. Organic Petrology. Borntraeger, Stuttgart (704pp).
Walter, M.R., Veevers, J.J., Calver, C.R., Grey, K., 1995. Neoproterozoic stratigraphy of the Centralian Superbasin, Australia. Precambrian Res. 73, 173–195. http://dx.doi.org/10.1016/0301-9268(94)00077-5.
Warr, L.N., Ferreiro Mählmann, R., 2015. Recommendations for Kübler Index standardization. Clay Miner. 50, 283–286.
Warr, L.N., Rice, A.H.N., 1994. Inter-laboratory standardization and calibration of clay mineral crystallinity and crystallite size data. J. Metamorph. Geol. 12, 141–152.
Weaver, E.W., 1960. Possible uses of clay minerals in search for oil. Bull. Am. Assoc. Pet. Geol. 44, 1505–1518.
Wopenka, B., Pasteris, J.D., 1993. Structural characterization of kerogen to granulite-facies graphite: applicability of Raman microprobe spectroscopy. Am. Mineral. 78, 533–557.
Zieger, L., Littke, R., Schwarzbauer, J., 2018. Chemical and structural changes in vitrinites and megaspores from carboniferous coals during maturation. Int. J. Coal Geol. 185, 91–102. http://dx.doi.org/10.1016/j.coal.2017.10.007.